WIRELESS POWER TRANSFER FOR MEDICAL AND INDUSTRIAL APPLICATIONS

by

NGUYEN QUOC MINH

Presented to the Faculty of the Graduate School of

The University of Texas at Arlington in Partial Fulfillment

of the Requirements

for the Degree of

DOCTOR OF PHILOSOPHY

THE UNIVERSITY OF TEXAS AT ARLINGTON

May 2016

Copyright © by Nguyen Quoc Minh 2016

All Rights Reserved

Acknowledgements

I would like to express my appreciation and thankfulness to my supervisor Professor Jung-Chih Chiao. Without his guidance and persistence help, this dissertation would not be possible. His support and encouragement was never ending. I also would like to thank Dr. Wei-Jen Lee, Dr. Michael Vasilyev, Dr. Alan Davis and Dr. William Dillon for being my dissertation committee.

A special thanks to all of my friend at UT-Arlington and iMEMS group, especially Hung Cao, Cuong Nguyen and Souvik Dubey for their consistent help and support. I have gained a lot of knowledge and experience from them during my period. I also would like to thank Smitha Rao for her valuable suggestions in my research.

Last but not least, I want to thank my parents, parents in law, my wife - Anh Pham and my son - Ryan Nguyen for their endless love and support.

April 5, 2016

Abstract

WIRELESS POWER TRANSFER FOR MEDICAL AND INDUSTRIAL APPLICATIONS

Nguyen Quoc Minh, PhD

The University of Texas at Arlington, 2016

Supervising Professor: Jung-Chih Chiao

My primary research focuses on wireless power transfer technology utilizing in two different areas: medical and industrial applications.

In the medical applications, my research focuses on design and optimization methods for spiral coils utilized for wireless power transfer in wireless medical implant applications. A theoretical model was examined for near field distributions of spiral-type transmitter antennas in both orthogonal components. Finite element simulations were performed to verify the theoretical radiation patterns. Receiver antenna voltages were measured at planes of interest as a means to map field distributions. Theoretical, simulation and experimental results were conducted in the free space and they agreed well. Understanding the orthogonal field components and their distributions in various distances between the worn transmitter coil outside the body and the receiver coil of implant that has a much smaller size provides a means to find the optimal location and angle to harvest maximum energy. The analysis method for near-field wireless power transmission can be utilized to determine design strategies of the transmitter spiral coil with also considerations in the amplifier circuit and physical constraints in practical scenarios to obtain maximum power and link efficiency for the implant devices. The method can be extended to investigate field distributions affected by human tissues, which construct a much more complex environment.

In the industrial applications, the effect of power combining and delivering in multi-input and multi-output (MIMO) wireless energy transmission systems which consist of more than one transmitter antennas as sources, more than one receiver antennas as loads and repeaters is investigated. Theoretical expressions were developed to model system operation that can be in a large scale wireless energy network architecture. System characteristics such as power transfer between antennas, power losses induced in each antenna, wireless efficiency, coil misalignment and power fluctuation due to the loss of frequency synchronization were examined by theory and verified with experiments. Measurement results matched well with the theory demonstrating the feasibility of combining and delivering power with high efficiencies in large scale wireless energy transmission systems.

Table of Contents

List of Illustrations

List of Tables

Chapter 1

INTRODUCTION

1.1 Literature Review

Wireless power transfer (WPT) is a transmission of electrical power from a source to a load without physical contact. The idea of transmitting power wirelessly was first introduced by Nikola Tesla in 1906. In his experiment, he used two power towers to transfer the power wirelessly over long distance. Although his experiment didn't get significant attention at that time, Tesla made a prediction that wireless power transfer would become industrial revolution. In 2006, 100 years after Tesla's experiment, a research group from MIT gained immediately attention by demonstrating a system transferring wireless power to light up a 60W bulb over a distance of 2m with an efficiency of 40% [39].

1.1.1. Basic principle

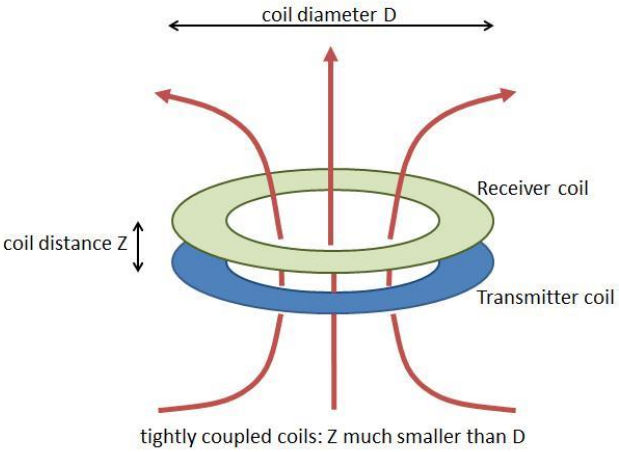

Figure 1-1 Inductive coupling between antennas

[https://www.wirelesspowerconsortium.com/technology/magnetic-resonance-and-magnetic-induction-making-the-right-choice-for-your-application.html]

The principal of WPT is based on the inductive coupling between antennas. The key parameter in a WPT system is the coupling coefficient between antennas. The coupling coefficient determines the percentage of flux captured by the receiver which is generated by the transmitter. Therefore, coupling coefficient ranges from 0 to 1. In power transformer, coupling coefficient between primary coil and secondary coil is near unity since metal core is used as waveguide. In WPT, the coupling coefficient is normally less than 20% due to large amount of flux linkage through the air. In general, the transmission distance (d) is the practical limitation since electromagnetic waves attenuate at a rate of d^3 in the near-field coupling region. Therefore, transfer power and efficiency attenuate quickly as the distance increases. In addition to the limited distance, the misalignment is also a major issue since it determines the coupling between antennas.

1.1.2. WPT in medical applications

Wireless power transfer technology gains significant attention recently due to its numerous advantages in medical and industrial applications. Applications range from milliwatts for medical implants to ten of watts for consumer electronics and kilowatts for wireless powered electric vehicles. Powering the medical implant is the main challenge due to the size restriction of the devices. Several methods have been used for implant systems. The first method is the use of physical wire connection. This method is not preferred due to the high possibility of infection. Second method is the use of non-rechargeable battery to power the implant chip. This method shows advantage over wired connection method by minimizing the risk of infection. However, those batteries have limited life circle and need to be replaced by surgery at the end of its cycle. In addition, the size of the battery is also large since it usually includes charging capacitor. This creates complication and increases the cost of treatment. Therefore, many patients cannot afford

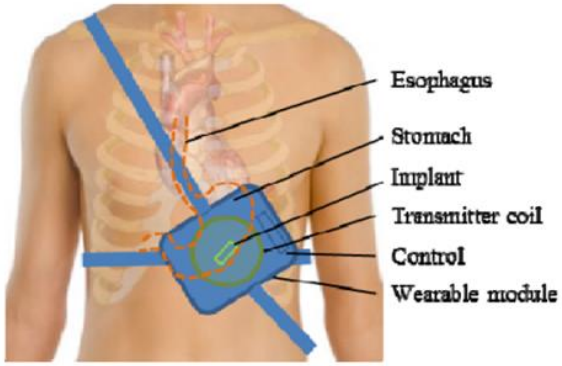

Figure 1-2 The concept of a WPT system for medical implant applications

the treatments. WPT has been increasingly involved in many applications recently such as pacemaker and gastrostimulator [1-4], bladder volume monitoring [5], cardiac implant [6,7]. In such applications, WPT have shown huge advantages over traditional battery-based implant devices by reducing the implant size, eliminating the associate battery for powering the devices and therefore, reducing cost of treatment. A typical setup of the WPT system for implant applications is shown in Fig. 1-2 [34]. In such system, an external reader is worn outside the body and powered by battery. The reader generates near-field electromagnetic waves which can propagate though human tissues in radio frequency band. Inside the body, a small coil harvests the energy and powers the functional components in the implant devices. In term of energy harvesting, such small coil could have a dimension of several mm to few cm, therefore, the overall size of the implant chip is significantly reduced.

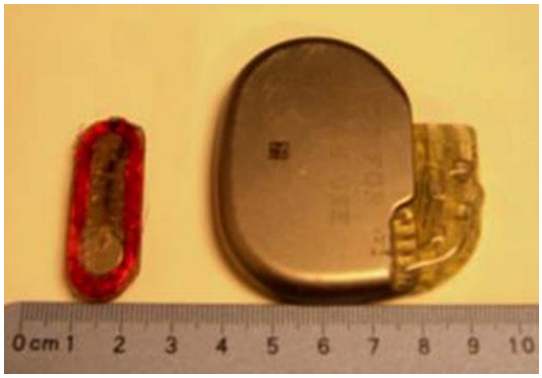

Figure 1-3 Wireless gastric stimulator (left) and battery-based Enterra@ stimulator (right)

In Fig. 1-3 [4,61], the size of the wireless gastrostimulator was reduced to 9×37mm to compare with 55×60mm of the Enterra@ developed by Medtronix, Inc. Although WPT brings a lot of benefits to the medical, the practical challenge is identified as the misalignment issue between transmitter worn outside the body and receiver implanted inside the body [8,16]. Once the device is implanted, misalignment may be due to patient's daily activity or stomach's activity. Under severe misalignment condition, implant might not receive enough power to operate and affect the treatment. Several research investigated the misalignment effect between TX and RX [15,16]. However, the misalignment is only examined either in lateral or angular condition due to the complexity of the analytical expression. it still lacks of literatures on examining the misalignment in both lateral and angular conditions, which is more practical. In addition, the designing and optimizing of the antenna to deal with misalignment conditions are also limited.

1.2.3. WPT in industrial applications

In addition to the medical applications, WPT also become more and more involves in consumer electronic applications such as cellphones and laptops [28-30]. Fig. 1-4 shows the charging station for cellphone developed by Samsung. In such applications, the distance between TX and RX is normally in short range of 4-10cm so that the efficiency is

Figure 1-4 Wireless charging for cell phones [http://www.androidcentral.com/dual-wireless-charging-samsung-galaxy-s6-and-why-it-matters]

sufficient large. When the distance increases, the transfer power and system efficiency attenuates quickly making the system inoperable. Several methods have been used to improve the transfer power as well as efficiency over long distance. In [44], ferrite-core antennas were used to improve the transfer efficiency between TX and RX. The ferrite helps to enhance the magnetic field intensity along the core and therefore improve the coupling coefficient significantly [44]. The results show that the efficiency can be achieved nearly 90% at 5-m distance by using optimal-shaped ferrite core. However, the length of the ferrite core is also relatively large and makes it difficult to implement in practical system [44]. In addition to the use of magnetic materials, the use of repeaters also gains a lot of attention recently. Studies show that the efficiency can be enhanced significantly over long range by using repeater antennas [40,52,53,57]. The repeater is usually placed in between TX and RX and act as power hubs to harvest the power from TX and then redeliver the power to RX with high efficiency. The optimal number and position of repeaters can be obtained directly from equivalent inductive coupling circuit theory [52,53]. The results show that the optimal position of repeaters is slightly offset from equal spacing between antennas

in a straight arrangement due to the cross coupling effect between non-adjacent antennas [52]. In [57], 17 repeaters were used to transfer the power at the overall distance of 5m with an efficiency of 40%.

1.2.4. Advanced system architectures

Although multiple repeaters were used to enhance the transfer distance [57], such systems are still classified as single-input and single-output systems since the power only enters to TX and delivers to RX while repeaters act as passive devices to guide the magnetic field from TX to RX. The number of powered devices is limited at one. The demand for charging multiple devices simultaneously becomes critical, especially for home and office applicants. Several works investigated the system operation with either multiple TXs or multiple RXs [45-49,70]. In such systems, the power is transferred directly from single TX to multiple RXs or from multiple TXs to single RX. However, it still lacks of literature on system implementing diversity on both TX and RX sides. Therefore, the feasibility of extending the system to a larger scale, which includes multiple TX and multiple RX is limited.

1.2 My Contributions

My research focuses primarily on two areas for utilizing WPT technology: 1. Medical and 2. Industrial applications. The main difference between these two areas is the size of the antennas.

For wireless power transfer system targeting medical applications, the receiver antenna size is strictly limited because of the implantable requirement. The challenges are further elevated as the doctor or patient could not identify the implant location or orientation easily in regular out-patient or home settings. Misalignment in position and angle becomes critical as the electromagnetic energy in conventional inductive coupling decays quickly

with distance. This study focuses on optimizing near field distribution pattern and power beam of transmitter antenna which helps to deal with the misalignment issue between transmitter and implant.

For wireless power transfer system targeting industrial applications, the antenna size is relatively large in order to receive enough power to operate consumer electronics. In this study, a new network architecture which can harvest wireless power from multiple transmitters and deliver the power to multiple receivers at high efficiency is proposed. In such systems, repeaters are used as indirect paths for energy exchange between antennas, which can reduce power loss and enhance system efficiency significantly over long distance. The frequency splitting phenomenon in WPT system is also investigated. The results show that the transfer power is maximized at low mode and high mode frequencies instead of self-resonant frequency of the system in near distance. When the distance increases beyond a critical value, two modes converge at self-resonant frequency of the system. Understanding these modes can help to design and operate the system so that the maximum possible transfer power is always achieved.

1.3 Dissertation Organization

Chapter 2 presents a near field distribution model of spiral antenna for misalignment analysis in wireless medical implant systems. In this session, horizontal and vertical components of magnetic field generated by spiral transmitter antennas at different spacing are obtained analytically. The calculated field intensity is then verified by both finite simulation element in ANSYS HFSS and experiment. In experiment setup, the receiving voltage captured from receiver is normalized to the percent value in order to compare with the normalized magnetic field. From the field distribution analysis, the optimization of antenna design to obtain maximum transfer power and efficiency is also given.

In chapter 3, a new wireless power system architecture which can harvest the power from multiple TXs and deliver the power to multiple RXs is proposed. Equivalent circuit theory is given to model the system in a large scale network architecture. From the theory model, input and output power, power loss in each antenna, power transfer between antennas and system efficiency are obtained. The system performance is verified by a prototype system consisting two TXs, two RXs and a repeater. The extension of 2×2 system to a larger 4×6 system is also investigated.

In chapter 4 the frequency splitting phenomenon in WPT system is studied. The splitting phenomenon is first examined in the conventional single-input and single-output system. The low and high mode frequencies are obtained from eigenvalue analysis. The frequency splitting is further examined in a prototype MIMO system consisting 2 TXs, 2 RXs and a repeater and multiple frequency modes are observed. These modes are obtained directly from theory and verified by experimental validation. Additional insertion losses are observed due to the skin and proximity effect of multi-turn conductor at high frequency.

Chapter 2

WIRELESS POWER TRANSFER FOR MEDICAL APPLICATIONS

2.1 Introductions

This chapter presents design and optimization methods for antenna design used for wireless power transfer in wireless medical implant applications. A theoretical model was examined for near field distributions of spiral-type transmitter antennas in both orthogonal components. Finite element simulations were performed to verify the theoretical radiation patterns. Receiver antenna voltages were measured at planes of interest as a means to map field distributions. Theoretical, simulation and experimental results were conducted in free space and they agreed well. Understanding the orthogonal field components and their distributions in various distances between the worn transmitter coil outside the body and the receiver coil of an implant that has a much smaller size provides a means to find the optimal location and angle to harvest maximum energy. The analysis method for near-field wireless power transmission can be used to determine design strategies of the transmitter spiral coil with also considerations in the amplifier circuit and physical constraints in practical scenarios to obtain maximum power and link efficiency for the implant devices. The method can be extended to investigate field distributions affected by human tissues, which construct a much more complex environment, and will be conducted in future works.

Wireless power transfer technology provides unique features and thus has been greatly involved in various industries recently, especially in medical applications. Wirelessly-powered or wirelessly-charged implants feature many advantages over traditional wire-tethered or non-rechargeable battery types of diagnostic or therapeutic devices by providing comfort to patients in chronic usages, reducing implant sizes which reduces incision dimensions or makes it possible for endoscopic implantation, and

eliminating frequent battery replacement surgeries. Advances have been achieved with wirelessly-powered implants for gastroesophagus reflux monitoring applications [1-3], gastrostimulators in management of gastroparesis and stomach motility disorders [4], bladder volume monitoring in incontinence management [5], cortical implants for monitoring neural activities [6] and cardiac implants [7]. These applications demonstrated the advantages of batteryless wireless medical devices and enhanced performance in potential clinical uses.

In general, wirelessly-powered implant systems require proper alignment between the transmitter and implant (receiver) antennas to receive sufficient powers to operate the devices. The technical challenges faced are due to the significant difference in transmitter and receiver antenna sizes since the implant dimensions are often strictly limited, especially for the ones applied in noninvasive or minimally invasive implantation procedures. The challenges are further elevated as the doctor or patient could not identify the implant location or orientation easily in regular out-patient or home settings. Thus, one may have trouble to precisely place the transmitter antenna, which often is embedded in a belt or clothes, held by hands or supported with a bedside apparatus, in the correct or optimal position outside the body. Relative body motions in daily activities or organ/tissue movement also create uncertainty in estimating the implant position from outside the body. Misalignment in position and angle becomes critical as the electromagnetic energy in conventional inductive coupling decays quickly with distance. A radical and angular misalignment analysis for circular transmitter antennas has been examined in detail by Nguyen, et al.[8]. Recent studies showed that using spiral structures for the transmitter antenna can significantly improve the wireless power transmission and have a better beam size for the receiver antenna [9].

In this chapter, theories are examined to analyze the radiation patterns of spiral coils. The work focuses on developing a mathematical model to analyze the near-field distributions and optimize the designs of spiral coils to achieve maximum power transfer and system efficiency. The theory model was validated by simulations with finite-element High Frequency Structure Simulator (HFSS) and experimental results. The near field distributions of orthogonal field components were examined so that an optimal location and angle of the receiver coil with respect to the transmitter coil could be determined to harvest maximum energy at different distances between the coils.

2.2 Antenna Structure and Near Field Theory Model

A spiral coil antenna (Fig. 2-1(a)) can be mathematically represented in the Cartesian coordinate system as [33]:

$$x(\theta) = a\theta\cos\theta,\ y(\theta) = a\theta\sin\theta \tag{2.1}$$

where *a* is a constant to control spacing and θ is the angle from the x axis. Spacing between adjacent turns can be obtained as:

$$d = x(\theta + 2\pi) - x(\theta) = 2\pi a \tag{2.2}$$

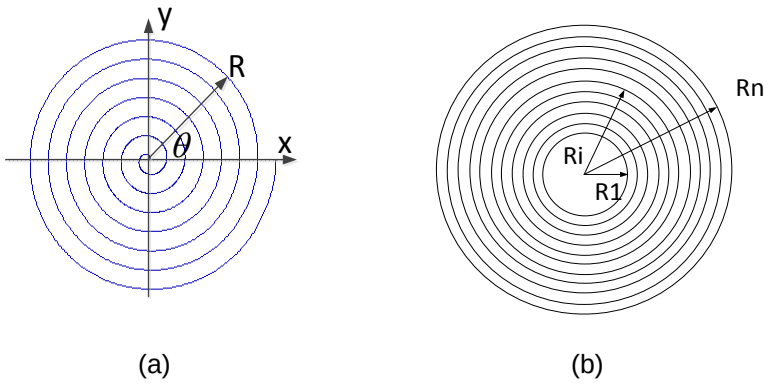

(a) (b)

Figure 2-1 (a) Spiral coil antenna configuration and (b) its equivalent concentric-loop model

To establish a theoretical field distribution model for Eq. 2.1 is difficult. An approximation approach considers a spiral coil as superposed multiple concentric, circular loops with various radii [10], as shown in Fig. 2-1(b) [33]. The field distributions of such a simplified model can then be derived from fields superposition generated by loop currents. The simplified model allows a quick estimate of power distribution of similar spiral coils. Assume the electrical current is uniformly distributed through the loop as the wavelength of the carrier signal is much longer than the loop perimeter. In such a case, the vector potential A in terms of A_ϕ, A_ρ and A_z at the location W in Fig. 2-2 [33] in a cylindrical coordinate system (ϕ, p, z) can be derived as [11]:

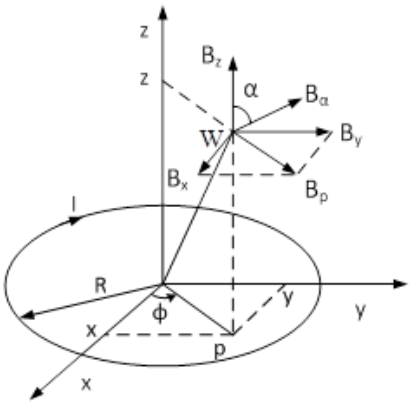

Figure 2-2 Magnetic field vector by a circular electrical current

$$A_\phi = \frac{\mu I}{4\pi}\int \frac{ds}{r} = \frac{\mu I}{4\pi}\int_0^\pi \frac{R\cos\phi d\phi}{(R^2+p^2+z^2-2Rp\cos\phi)^{\frac{1}{2}}},\ A_p = 0,\ A_z = 0 \qquad (2.3)$$

where R is the coil radius; p and z are the displacements in horizontal and vertical directions in the cylindrical coordinate system; I is the current flowing in the coil. After substituting the variable ϕ with $\pi+2\theta$ for the spiral antenna, the potential A_ϕ becomes:

$$
\begin{aligned}
A_\phi &= \frac{\mu R I}{\pi}\int_0^{\frac{\pi}{2}} \frac{(2\sin^2\theta - 1)d\theta}{(R^2 + p^2 + z^2 - 4Rp\sin^2\theta)^{\frac{1}{2}}} \\
&= \frac{k\mu I}{2\pi}\left(\frac{R}{p}\right)^{\frac{1}{2}}\left[\left(\frac{2}{k^2} - 1\right)\int_0^{\frac{\pi}{2}} \frac{d\theta}{\sqrt{1-k^2\sin^2\theta}} - \frac{2}{k^2}\int_0^{\frac{\pi}{2}} \sqrt{1-k^2\sin^2\theta}\, d\theta\right] \\
&= \frac{\mu I}{\pi k}\left(\frac{R}{p}\right)^{\frac{1}{2}}\left[\left(1 - \frac{1}{2}k^2\right)K(k) - E(k)\right]
\end{aligned}
\tag{2.4}
$$

where *K(k)* and *E(k)* are the complete elliptical integrals of the first and second kinds to the modulus *k*, respectively, and

$$
k^2 = 4Rp\left[(R+p)^2 + z^2\right]^{-1} \tag{2.5}
$$

$$
K(k) = \int_0^{\frac{\pi}{2}} \frac{d\theta}{\sqrt{1-k^2\sin^2\theta}}, \quad E(k) = \int_0^{\frac{\pi}{2}} \sqrt{1-k^2\sin^2\theta}\, d\theta \tag{2.6}
$$

The magnetic field components can then be calculated from the vector potential as:

$$
\begin{aligned}
\mu_0 H_p = B_p &= -\frac{1}{p}\frac{\partial}{\partial z}(pA_\phi) + \frac{1}{p}\frac{\partial}{\partial \phi}(A_z) = -\frac{\partial A_\phi}{\partial z} \\
\mu_0 H_\phi = B_\phi &= \frac{\partial}{\partial z}(A_p) - \frac{\partial}{\partial p}(A_z) = 0 \\
\mu_0 H_z = B_z &= -\frac{1}{p}\frac{\partial}{\partial \phi}(A_p) + \frac{1}{p}\frac{\partial}{\partial p}(pA_\phi) = \frac{1}{p}\frac{\partial}{\partial p}(pA_\phi)
\end{aligned}
\tag{2.7}
$$

By substituting Eq. 2.4 into Eq. 2.7, the horizontal and vertical (with respect to the coil cross section) components of magnetic fields created by a circular current can be represented as:

$$
\begin{aligned}
H_p &= \frac{1}{\mu_0}\frac{\mu I}{2\pi}\frac{z}{p[(R+p)^2 + z^2]^{1/2}}\left[-K(k) + \frac{R^2 + p^2 + z^2}{(R-p)^2 + z^2}E(k)\right] \\
H_z &= \frac{1}{\mu_0}\frac{\mu I}{2\pi}\frac{1}{[(R+p)^2 + z^2]^{1/2}}\left[K(k) + \frac{R^2 - p^2 - z^2}{(R-p)^2 + z^2}E(k)\right]
\end{aligned}
\tag{2.8}
$$

With an angle of α relative to the z-axis (Fig. 2-2), the magnitude of the magnetic field component in the α direction could be expressed as:

$$H_\alpha = \left| H_p \sin\alpha + H_z \cos\alpha \right| \tag{2.9}$$

In free space, $\mu = \mu_0$ .In the Cartesian coordinate system, the magnetic fields are:

$$H_x = H_p \cos\phi, \;\; H_y = H_p \sin\phi, \;\; H_z = H_z \tag{2.10}$$

On the z-axis where p=0, the components become:

$$H_x = 0, \;\; H_y = 0, \;\; H_z = \frac{1}{2}\frac{R^2 I}{(R^2 + z^2)^{3/2}} \tag{2.11}$$

The magnetic field intensity of a spiral coil then can be approximated as:

$$H_x = \sum_{1 \le i \le n} H_{xi}, \;\; H_y = \sum_{1 \le i \le n} H_{yi}, \;\; H_z = \sum_{1 \le i \le n} H_{zi} \tag{2.12}$$

where H_{xi}, H_{yi} and H_{zi} are the horizontal and vertical components of magnetic fields created by the ith loop in which the radius R *is* R_i, the radius of the ith loop.

Two transmitter coils were considered with their parameters shown in Table 2-1. The parameters were used to calculate the magnetic field distributions. Figures 2-3 and 2-4 show the magnetic field component (H_z and H_x) distributions at the cross-section planes with spacings of 5 cm, 7 cm and 10 cm to the spiral coils [33].

Table 2-1 Transmitter Coils

Parameters	TX Antenna	
	Coil 1	Coil 2
Inner radius (cm)	11	4
Outer radius (cm)	18	18
Turn number	10	10
Turn spacing (mm)	7.778	15.556
Average radius (cm)	14.5	11
Material	Litz wires	Litz wires

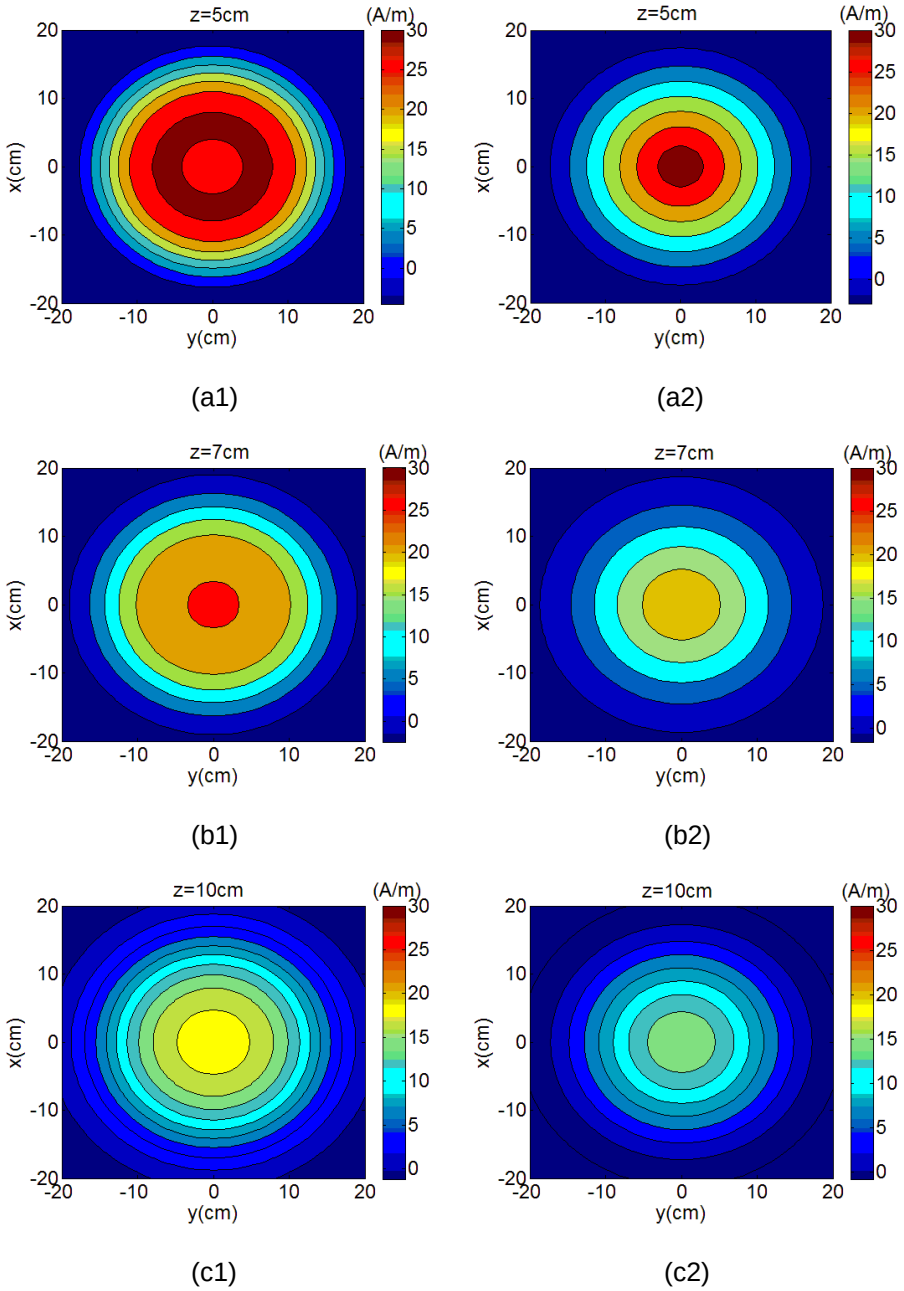

Figure 2-3 Radiation patterns of vertical components (Hz) for two spiral antennas (Coil 1 (a1,b1,c1) and Coil 2 (a2,b2,c2)) at three planes parallel to the coil antenna with distances (z) of 5 cm (a1,a2), 7 cm (b1,b2) and 10 cm (c1,c2) to the coil

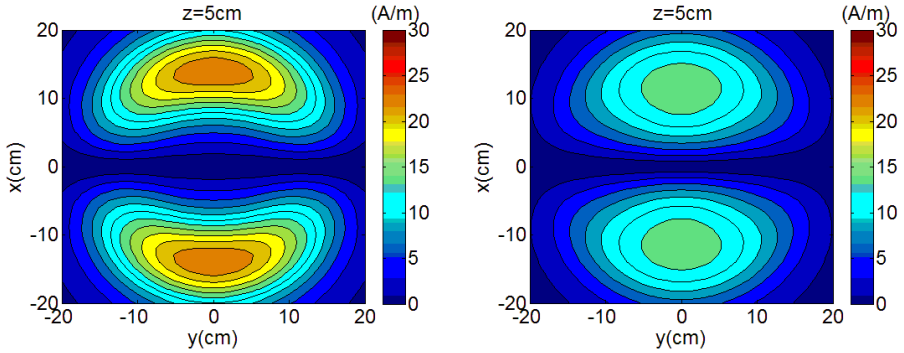

(a1)

(a2)

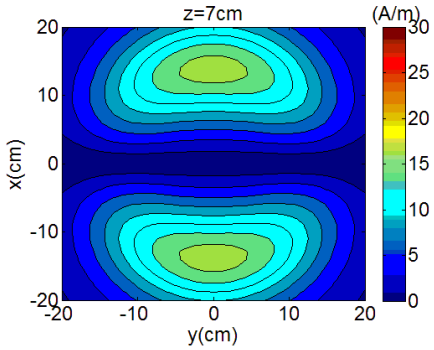

(b1)

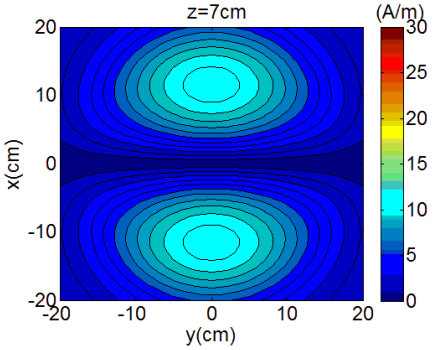

(b2)

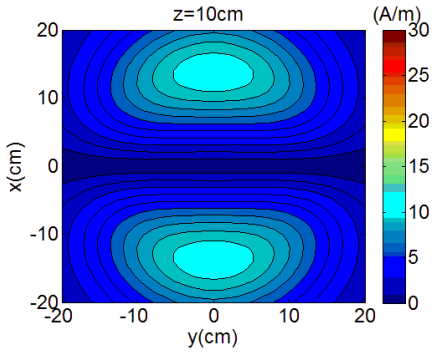

(c1)

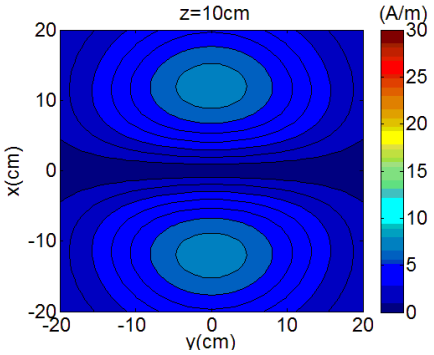

(c2)

Figure 2-4 Radiation patterns of horizontal components (Hx) for two spiral antennas (Coil 1 (a1,b1,c1) and Coil 2 (a2,b2,c2)) at three planes parallel to the coil antenna with distances (z) of 5 cm (a1,a2), 7 cm (b1,b2) and 10 cm (c1,c2) to the coil

The colors indicate the magnitudes of magnetic fields H when an electrical current of 1A flows in the coil wires. The outer radius of both coils is 18 cm. The cross section of interest is ±20 cm in both x and y directions with (x=0, y=0) aligned with the center of the transmitter spiral coil.

The H_z component patterns indicate that the magnetic fields are concentrated near the center area. The pattern for the H_x component, on the other hand, is mostly distributed at the outer areas with much lower field intensity in the center. The H_y component pattern is expected to be similar to the ones for H_x, except the patterns rotate by 90^o with the field nulls along the y=0 axis instead of x=0 axis. The field patterns are important to determine the optimum position of the implant coil where the harvested energy is maximized considering both position and angular arrangements. When the receiver coil is perfectly in parallel to the transmitter coil, the implant receiver that has a much smaller size will only harvest the energy in H_z. As the receiver coil pivots itself, along any axis through the coil surface but orthogonal to the normal vector of the coil surface, to have a misalignment angle relative to the transmitter coil, the receiver coil receives energy partially from H_z and partially from H_x and H_y. The total received energy then depends on the misalignment angle as well as the relative location of the receiver coil. This type of scenarios often happens because it is difficult to maintain a perfect parallelism between the implant coil which is inside the body, and the transmitter coil which is outside the body.

The relation between the optimal position p_{opt} where the receiver coil receives the maximum energy and the misalignment angle which was varied from being in parallel to completely orthogonal, was investigated in the planes at different distances (z) of 5, 7 and 10 cm between the transmitter and receiver coils. The results are shown in Fig. 2-5 [33]. The optimum position p_{opt} is defined as the distance, in the plane of interest, from (x=0, y=0) that is aligned to the center of the transmitter coil to the receiver coil center.

For the transmitter Coil 1, the receiver coil does not receive the maximum energy at (x=0, y=0) when the coils are facing each other at a distance of 5 cm. As the receiver coil moves to a distance of 6.4 cm from the center, the received energy becomes maximum (Fig. 2-5(a)). This is expected as the magnitude of H_z reaches maximum, instead in the center, at 6.4 cm away from the center. At the distance of 5 cm, the superposed magnetic fields from the multiple loops in the spiral coil add up more near the center of the cross-section plane, instead of the center, making the field distribution a donut shape. This phenomenon does not exist for Coil 2 at the distance of 5 cm. The main difference between these two coils with the same turn and outer radius is the loop spacing between adjacent wires in the loop. It is obvious that the design parameters in spiral coils will be critical depending on the inductive coupling distance, even for perfectly aligned antennas. For Coil 1 and with the distances of 7 and 10 cm, the optimal positions for the perfectly aligned coils are in the center as the maximum magnetic fields are in the center of the plane, as the same for Coil 2.

When the receiver coil has a misalignment angle relative to from the transmitter coil, the optimal distance in Fig. 2-5 increases as the receiver coil moves toward the edge of the transmitter coil in the plane, as the receiver coil starts to receive energy from both H_z and H_x/H_y components.

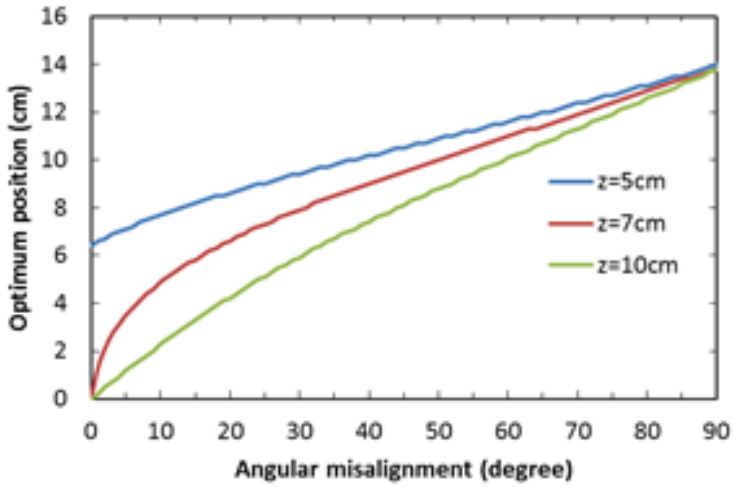

(a)

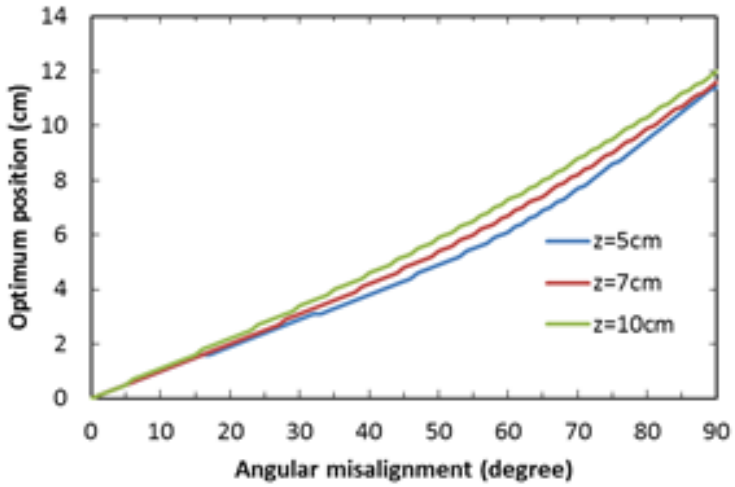

(b)

Figure 2-5 Optimal position to produce maximum harvested energy as a function of angular misalignment at three distances of 5, 7 and 10 cm between the transmitter and receiver coils. (a) Transmitter Coil 1. (b) Transmitter Coil 2. The optimal position is the distance, in the cross-sectional plane where the receiver coil locates, from (x=0, y=0) that is aligned to the center of the transmitter coil

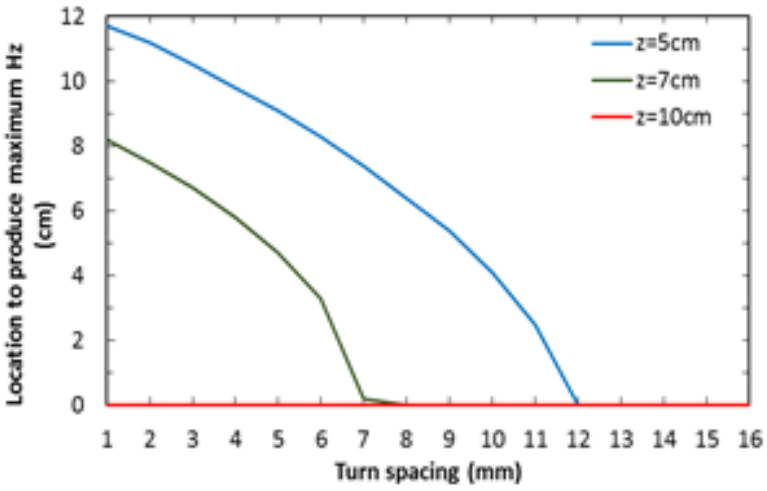

(a)

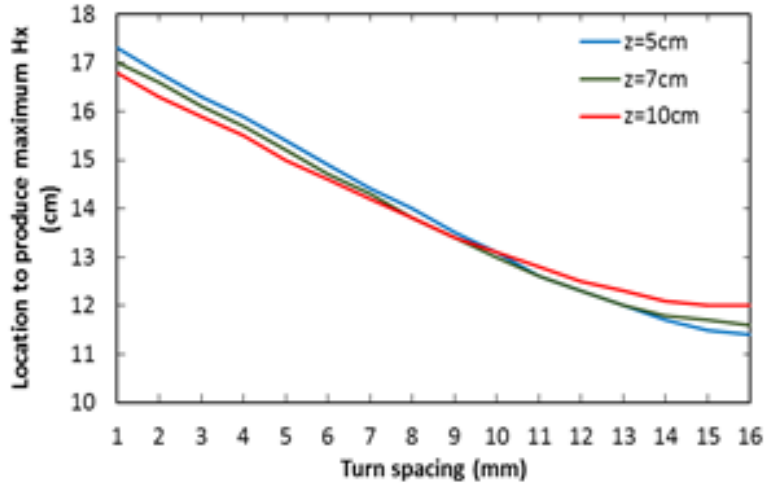

(b)

Figure 2-6 Location of maximum field intensity of (a) H_z and (b) H_x components as a function of turn spacing between wires for a spiral transmitter coil with an 18-cm outer radius and 10 turns. The location is the distance, in the cross-sectional plane where the receiver coil locates, from (x=0, y=0) that is aligned to the center of the transmitter coil

When the misalignment angle is 90°, the optimal positions for the receiver Coil 1 are 14, 13.8 and 13.8 cm from (x=0, y=0) for the spacings of 5, 7, and 10 cm, respectively. If the receiver coil is orthogonal to the transmitter coil, the energy harvested comes from H_x and H_y only. This is expected as shown in Fig. 2-4, the maximum field intensity of H_x in Coil 1 is near at ±14 cm from the center. As the distance between the transmitter and receiver coils increases, the location of the maximum field intensity of H_x seems to converge at around ±14 cm.

The turn spacing increases from 7.778 mm in Coil 1 to 15.556 mm in Coil 2, resulting in a decrease of the inner radius from 110 mm to 40 mm. If coils face each other in parallel, p_{opt} becomes zero at a spacing of 5 cm since the maximum of the H_z component remains in the center. This is likely due to the decrement of the loop size near the center in the spiral coil. When the receiver coil misalignment angle increases, the optimal location moves to the edge similar to the case for Coil 1. When the misalignment angle is 90°, the optimal positions for the receiver coil are 11.4, 11.4 and 12 cm from (x=0, y=0), as shown in Fig. 2-5(b). Coil 1 and Coil 2 have the same outer radius of 18 cm and same number of turns (10). The turn spacing between loop wires thus determine the field distribution shapes in the near field – either a single peak or donut shapes.

Figure 2-6 [33] shows the changes of location where the maximum field intensity is due to the turn spacing increase from 1 to 16 mm. As the turn spacing increases, the loop becomes smaller in the center and the optimal position to produce maximum H_z intensity moves toward the center, as shown in Fig. 2-6(a). That maximum location distance from the center also decreases significantly since the coil spacing distance increases. The maximum H_x location moves from the edge (around 17 cm) toward the inner area (around 11.5 cm) when the turn spacing increases from 1 to 16 mm. The maximum

H_x location, on the other hands, is not sensitive to the coil spacing distance, as shown in Fig. 2-6(b).

2.3 Finite Element Simulation

A simulation model was developed in HFSS (High Frequency Structure Simulator) to verify the theory. The spiral shapes of Coil 1 and Coil 2 (Fig. 2-7) were generated with Eq. 2.1 [33]:

$$x(\theta) = a\theta\cos\theta,\ y(\theta) = a\theta\sin\theta,\ z(\theta) = 0$$
$$\theta_{start} = 2\pi \times N_{start},\ \theta_{stop} = 2\pi \times N_{stop} \tag{2.13}$$

where θ_{start} and θ_{stop} are the starting and ending angles; N_{start} *and* N_{stop} are the starting and ending turns. The configurations for each coil design in HFSS are given in Table 2-2. The port was excited with a current source with an amplitude of 1A. The vacuum was used as the propagation medium. Frequency was chosen at 1.3MHz. Field components were recorded at three planes of z = 5, 7 and 10 cm from the transmitter coil.

Table 2-2 Spiral Coil Configuration in HFSS

Parameters	TX Antenna	
	Coil 1	Coil 2
a (mm)	7.778/2π	15.556/2π
N_{start}	14	2
N_{stop}	24	12
θ_{start} (rad)	28π	4π
θ_{stop} (rad)	48π	24π

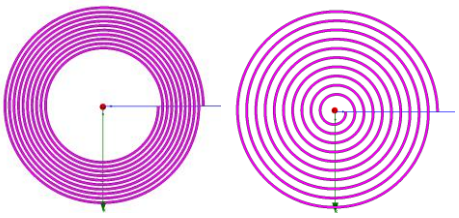

(a) (b)

Figure 2-7 Spiral coil designs in HFSS for (a) Coil 1 and (b) Coil 2

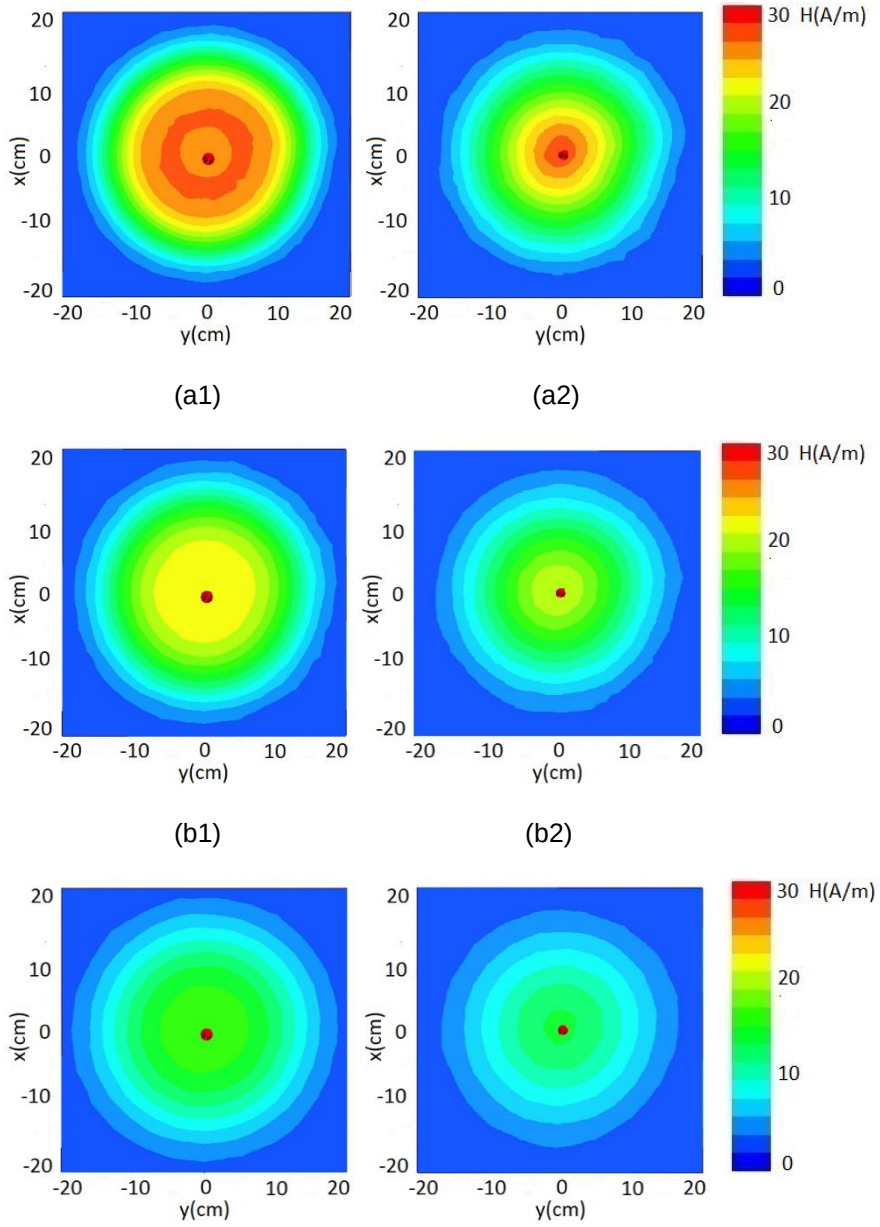

Figure 2-8 Field patterns of vertical components (Hz) in two spiral antennas (Coil 1 (a1,b1,c1) and Coil 2 (a2,b2,c2)) at three planes parallel to the transmitter coil in the HFSS simulation with distances (z) of 5 cm (a1,a2), 7 cm (b1,b2) and 10 cm (c1,c2) to the coil

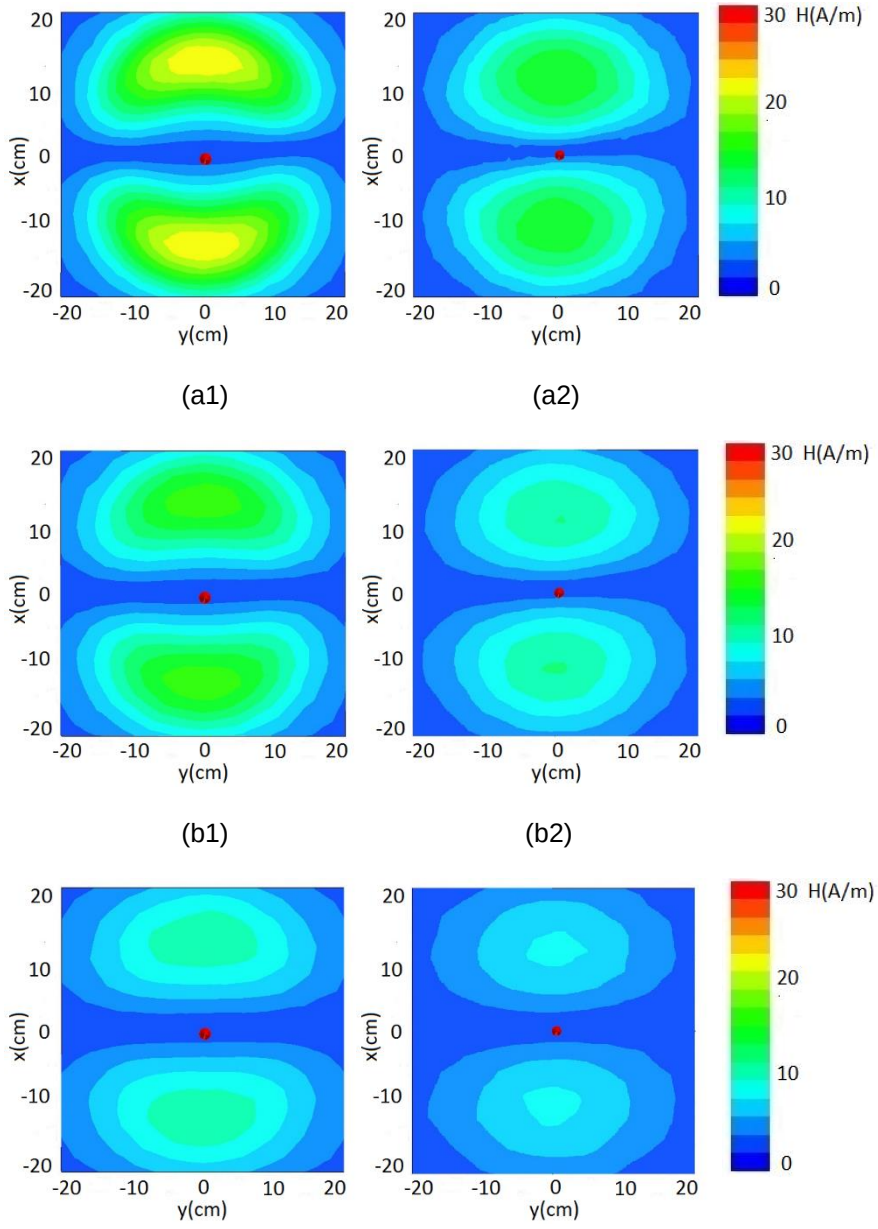

Figure 2-9 Field patterns of horizontal components (Hx) in two spiral antennas (Coil 1 (a1,b1,c1) and Coil 2 (a2,b2,c2)) at three planes parallel to the coil antenna in the HFSS simulation with distances (z) of 5 cm (a1,a2), 7 cm (b1,b2) and 10 cm (c1,c2) to the coil

The simulation field plots in Figs. 2-8 and 2-9 [33] match well with theoretical ones in Figs. 2-3 and 2-4. Thus the approximation by multiple concentric loops is appropriate to model the field distributions of the spiral antenna structures.

2.4 Experiments

Figure 2-10 [33] illustrates the equivalent circuit of the experiment setup. The system was designed at 1.3 MHz considering the recommended maximum permissible exposure of human tissue to magnetic fields is the highest in the 1.3 - 30 MHz band [27]. A class-E amplifier was used to generate a carrier at 1.3 MHz to feed the transmitter coil. The receiver coil was connected to a resistive load of 500 Ω. The load was chosen to mimic the stomach tissue impedance because the target application of our system is for gastrostimulation [4]. Coil 1 and Coil 2 were used as the transmitter antennas. The receiver coil antenna was made of 145-strand Litz wires with 10 turns. The resistivity of the Litz wire is 0.24 Ωm. The size of the receiver coil was limited to a 1.5-cm radius for potential endoscopic implantation of the implant through mouth and esophagus [4]. The thickness of the implant was determined by the turn number and limited to 5 mm, also for the purpose of endoscopic implantation. Therefore, the turn number was chosen as 10. The transmitter coil, represented as L_1 and tuning capacitor C_1 were connected in series, which can improve the power transfer significantly by fine tuning. The receiver coil L_2 was connected in parallel with the tuning capacitor C_2 to stabilize the voltage and reduce the noises and harmonics from the non-linear class E amplifier in the transmitter circuit.

An IRF510 (Fairchild) transistor was used in the class-E amplifier which was switched by a 6-V_{pp} square wave at a duty cycle of 50% from the Gate. A 4-V_{DC} from a DC power supply was fed into the Drain. The values of parameters used in experiment are given in Table 2-3.

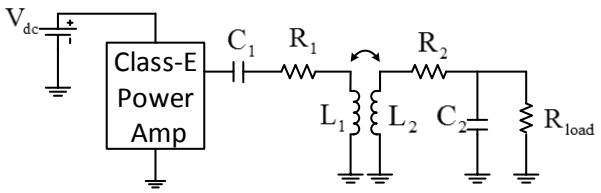

Figure 2-10 Circuit diagram of the experiment for the wireless power transfer system

Due to the symmetry, measurements were conducted one-dimensionally from the center of the measurement plane to the edge of the transmitter coil. The receiver coil was moved at an increment of 1.2 cm across a straight line, as shown in Fig. 2-11 [33], while the distance *z* was kept at 5, 7, and 10 cm from the transmitter coil.

Table 2-3 Experiment Setups

Parameters	TX Antenna		RX Antenna
	Coil 1	Coil 2	
Inductance (μH)	94.11	60.3	7.8
Resistance (Ω)	7.9	3.4	1
Matching capacitance (pF)	275	609	2556
V_{DC} (V)	4		
Load resistance (Ω)	500		
Frequency (MHz)	1.3		

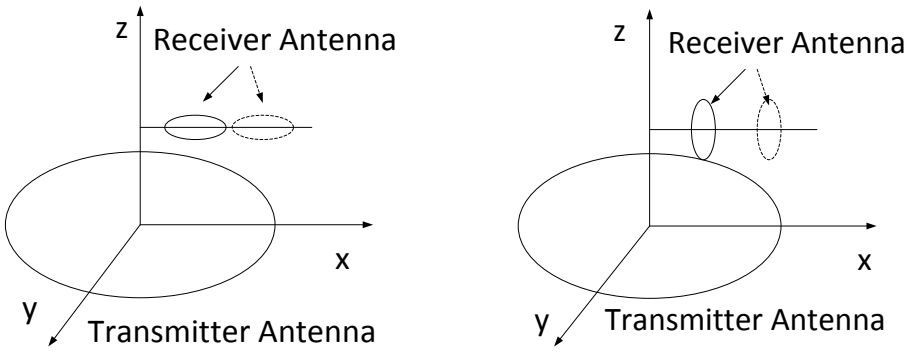

(a) (b)

Figure 2-11 Receiver coil with angular misalignments at (a) 0° and (b) 90° to the transmitter coil

The received output voltage is linearly proportional to the magnetic field intensity at the location of the receiver coil. Since the receiver coil size is much smaller than the transmitter coil, the magnetic fields created by the current flowing in the transmitter coil is considered to be uniformly distributed through the receiver coil cross section, only one field component which is normal to the plane of receiver coil induces voltage in the load. The magnetic fields calculated by theory and the measured output voltages were normalized to their respective maximum values for comparison.

Figures 2-12 and 2-13 [33] show the comparison between normalized calculated magnetic fields and measured load voltages with misalignment angles of 0^o and 90^o, respectively, for transmitter Coil 1 and Coil 2. At 0^o misalignment, the harvested voltage induced by the field component H_z mostly was distributed around the center area.

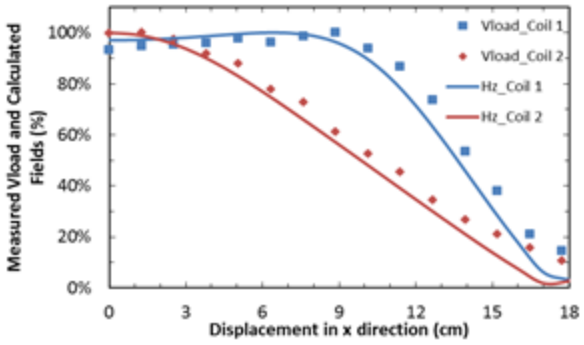

(a)

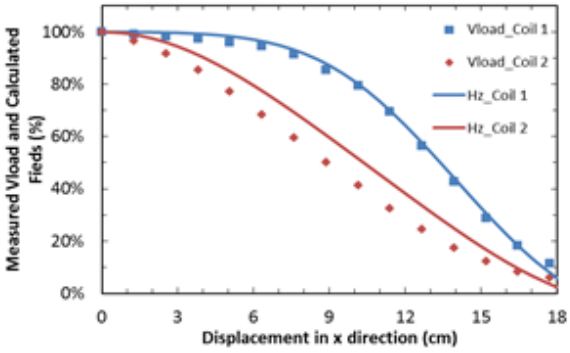

(b)

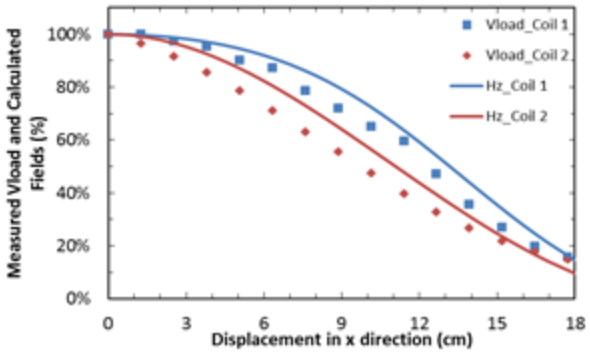

(c)

Figure 2-12 Theory and experiment results with normalized field components of H_z and measured output voltages at 3 distances of (a) 5, (b) 7, and (c) 10 cm between the transmitter coil and the plane of measurement when there is no angular misalignment

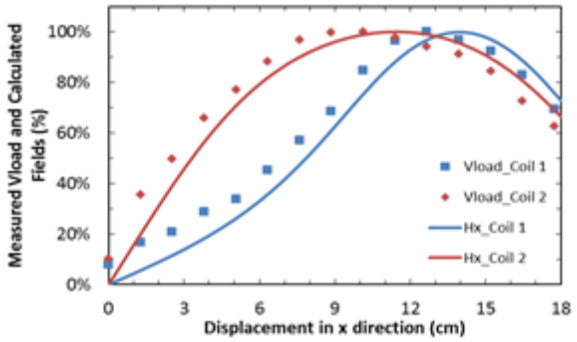

(a)

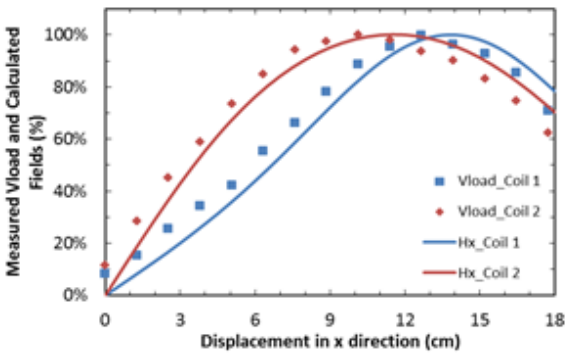

(b)

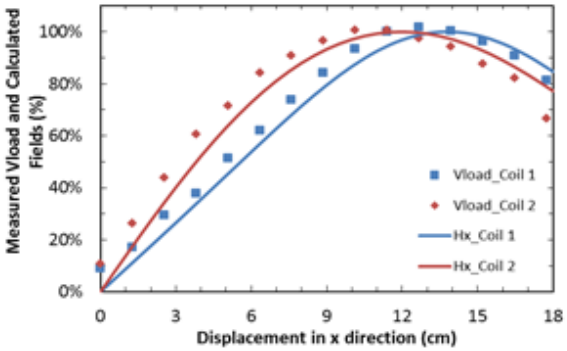

(c)

Figure 2-13 Theory and experiment results with normalized field components of H_x and measured output voltages at 3 distances of (a) 5, (b) 7, and (c) 10 cm between the transmitter coil and the plane of measurement when the angular misalignment is 90°

While Coil 1 was capable of maintaining 90% of the maximum field intensity within a 9-cm radius, Coil 2 can only maintain about 50% within the same area, as shown in Fig. 2-12(a). In other words, the H_z fields created by Coil 2 decay more quickly in the x direction than Coil 1. With a 90° misalignment angle, H_x field patterns concentrate around the outer area. However, the H_x fields created by Coil 1 vary more quickly in the x direction than Coil 2, as shown in Fig. 2-13(a). Figs. 2-12 and 2-13 show that the theory matches well with the experimental results so the theory can be used for design optimization.

2.5 Optimization of the Spiral Transmitter Coil

For a spiral coil, the geometric parameters determine the radiation patterns and can be optimized to obtain maximum power transfer and transmission link efficiency for particular requirements in targeted applications. With equal spacing between the loops and aligned coils, three parameters are considered: inner radius (R_{in}), outer radius (R_{out}) and turn number (N). In this section, a method to optimize the design of spiral antenna considering both field intensity and circuit efficiency is presented.

2.5.1 Determining of inner and outer radii

Assumed two coils are aligned in parallel so that only H_z components induce voltage. H_z is considered to be uniformly distributed through the receiver coil cross section because the transmitter coil is much larger than the receiver coil in dimensions. H_z depends only on the distance between two coils. The derivative of H_z component in Eq. 2.11 to find maximum

$$\frac{\partial H_z}{\partial R} = \frac{1}{2}\frac{2RI(R^2+z^2)^{\frac{3}{2}} - 3R^3I(R^2+z^2)^{\frac{1}{2}}}{(R^2+z^2)^3} \tag{2.14}$$

$$\frac{\partial H_z}{\partial R} = 0 \rightarrow R_{opt} = \sqrt{2}z \tag{2.15}$$

where R is the radius of transmitter coil and z is the distance between two coils.

Equation 2.15 indicates that there exists an optimum radius of the transmitter coil to maximize the field intensity in the plane of interest and, consequently, induced voltage in the load. Figure 2-14 [33] shows the H_z field intensity created by a 1-A loop current as a function of transmitter coil outer radius at three distances of 5, 7 and 10 cm. The figure shows both the optimal radius of coil to generate maximum fields and the relative scales of the field magnitudes at certain distance where the plane of interest locates. One needs to consider the tolerance in targeted applications when designing the coil. For example, if the target distance is 5 cm between the transmitter and receiver coils, an outer radius of 7.07 cm would be chosen for the transmitter coil to achieve maximum efficiency transfer with a field intensity of 3.85 A/m (indicated by “A” in Fig. 2-14). However, when the distance increases to 7 cm, due to many possible reasons such as body motion, misplacement of wearable coil on the body or gesture changes, the same coil will produce a field intensity of 2.54 A/m (indicated by “B”) while it further drops to 1.36 A/m at a distance of 10 cm (indicated by “C”). The field intensity varies almost 65% from the maximum of 3.85 A/m with a 5-cm distance change meaning a 65% change of harvested voltage. If a

coil radius of 9.90 cm is chosen, the field intensity becomes 3.59 A/m at the 5-cm distance (indicated by “D”) while it reaches maximum of 2.75 A/m (indicated by “E”) for the 7-cm distance case. When the distance increases to 10 cm, the field intensity becomes 1.76 A/m (indicated by “F”). The energy harvested at 5 cm is only 93% of the one when using the 7.07-cm radius coil, however, the field intensity varies 51% with a 5-cm distance change. In short, as the transmitter coil radius increases, the variation percentage of harvested energy becomes less giving more tolerance to distance variations. This is of course assuming that the harvested voltage is still above the requirement. For example, if the energy is only sufficient for a field intensity above 1.76 A/m (“F”), generated by 1-A current in the transmitter coil, to operate the circuit in the implant and the expected distance between two coils is less than 10 cm, the coil radius can be between 9.9 cm and 28 cm. It is desired to have a smaller wearable antenna, thus an appropriate coil radius is 9.9 cm.

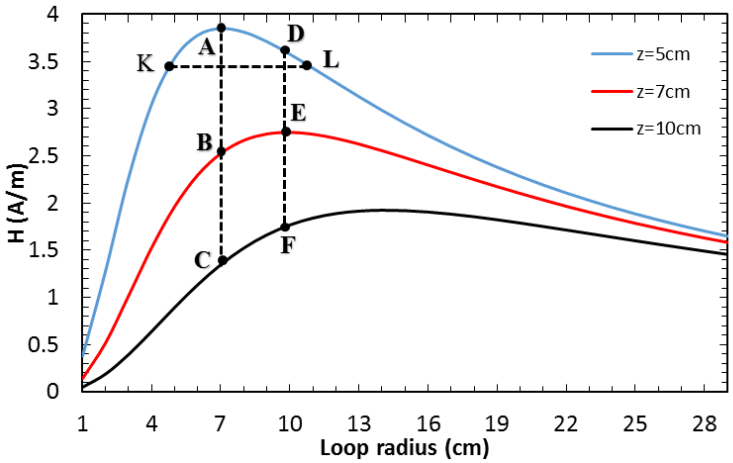

Figure 2-14 Magnetic field intensity as a function of transmitter coil radius at three distances of 5, 7 and 10 cm

However, if the desire is to minimize the voltage fluctuations due to spacing distance variations, a larger coil radius will be more appropriate. In the case when the distance

variation is not a major issue, energy transfer efficiency becomes more critical so that the coil radius should be as close to the R_{opt}. For example, if the required field intensity is greater than 3.5 A/m at the 5-cm distance, the transmitter coil radius can range from 4.9 cm (indicated by "K" in Fig. 2-14) to 10.5 cm (indicated by "L"), with 7.07 cm to reach the maximum efficiency. It would be a sensible choice to select 10.5 cm as the outer radius since the area coverage by the coil will be larger providing better spatial misalignment tolerance. The inner radius can theoretically be chosen from 4.9 cm to 10.5 cm in this case. A large inner radius will help to deal with the misalignment issue. Given a fixed turn number, a small inner radius is more sensitive to spatial misalignment, however, can reduce insertion losses in the transmitter circuit due to less electrical resistance in the shorter wire of coil. These are practical factors that need to be considered during the design process.

2.5.2 Determining of turn number

Conventionally, magnetic fields are considered to be proportional to the number of turns, therefore field intensity and received voltage can be increased by simply increasing the turn number. However, when turn number increases, the self inductance, mutual inductance and resistance will also increase and affect the equivalent circuits of the transmitter.

Inductance of spiral antenna can be calculated as [12]:

$$L = \mu_0 N^2 R_{avg} \left[\ln\left(\frac{2.46}{p}\right) + 0.2 p^2 \right] \tag{2.16}$$

where μ_0 is the magnetic permeability; p is the fill ratio as $p=(R_{out}-R_{in})/(R_{out}+R_{in})$; R_{avg} is the average radius as $(R_{out}+R_{in})/2$; and N is the turn number.

For coaxial filament loops, the mutual inductance between two coils can be calculated as [13]:

$$M = \mu_0 N_1 N_2 \sqrt{R_1 R_2} \left[(\frac{2}{k} - k)K - \frac{2}{k} E \right] \tag{2.17}$$

where R_1 and R_2 are the coil radii; N_1 and N_2 are the turn numbers; *K* and *E* are the complete elliptic integrals of the first kind and second kind to the modulus *k*, respectively, as represented in Eqs. 2.5 and 2.6.

Changing self-inductance will change the resonance condition and require corresponding matching capacitance. With a large inductance in a high turn number coil, the tuning capacitance may be so small that it can be affected easily by parasitic capacitance in the environment and circuits. Increasing the turn number will also increase the physical length of metal wire and the added resistance will apparently create more losses to the circuit and reduce the quality factor of the resonance. Therefore, the turn number needs to be optimized with respect to the equivalent circuit.

The efficiency of our wireless power transfer system can be represented as:

$$n\% = n_{PA}\% \times n_e\% \tag{2.18}$$

where n_{PA}% is the class-E amplifier efficiency and n_e% is the link efficiency.

Table 2-4 Simulation Parameters

Parameters	Coil	
	Transmitter	Receiver
Inner radius (cm)	4	1.5
Outer radius (cm)	10	1.5
Turn number	5 - 60	10
Inductance (μH)	Variable	7.8
Resistance (Ω)	Variable	1
Matching capacitance (pF)	Variable	2556
Load resistance (Ω)	500	
C_E (pF), L_E (μH)	1000, 100	
V_{DC} (V), V_F (V)	4, 6	
Distance (cm)	5	

Several analytical methods have been introduced to optimize the link efficiency [15,20,22] without considering the efficiency of the class-E amplifier due to its very high nonlinear characteristics. In this work, the class-E amplifier efficiency is considered with a simulation model since the transmitter coil is directly fed by the amplifier. The parameters of the transmitter, receiver coils and other components used in simulation are given in Table 2-4.

An equivalent circuit representing the coupled coils was considered with L_1-M, L_2-M and M components in the transmitter, as shown in Fig. 2-15 [33].

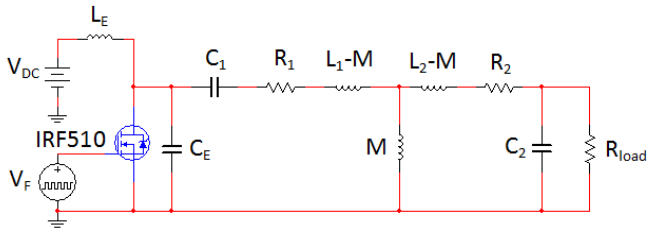

Figure 2-15 Simulated equivalent circuit of the transmitter

The equivalent circuit model was simulated in Multisim (National Instruments). In the wireless power transfer system, I used an n-channel high-efficiency low power switching MOSFET (IRF510) class-E amplifier to amplify the 1.3-MHz signal from a function generator. C_1 and C_2 are the matching capacitors in the transmitter and receiver tuning to resonance. C_1 was tuned to form a resonance circuit with the effective inductor L_1-M in the transmitter circuit while C_2 is fixed. Fixing C_2 is because the component values in the implant cannot be dynamically adjusted. R_1, R_2 and R_{load} are the equivalent resistances of transmitter coil, receiver coil and load, respectively. The values of L_1 and M are obtained from Eqs. 2.16 and 2.17, respectively, for different turns of the spiral transmitter coil while R_1 was assumed to be linearly proportional to the length of coil. The initial value of R_1 is 1.12 Ω at DC. The MOSFET was connected to a power supply through

an inductor L_E. The Drain and Source pins of the transistor were connected to a capacitor C_E. L_E and C_E formed an LC shunt circuit to ground. The Gate was triggered by a 1.3-MHz 50% duty-cycle square-waveform signal (V_F). Output voltage was probed at the load to calculate the output power while the input voltage and current from the DC supply were recorded to obtain the input power. System efficiency was calculated as the ratio between output and input powers, which included both wireless power transfer efficiency and the class-E amplifier efficiency.

Figure 2-16 [33] shows the results of simulation based on our theory. Given a DC input voltage of 4 V and fixed coil dimensions, there exists an optimal turn number of 15 to achieve the maximum load voltage of 5.95 V and another one of 35 turns for maximum power transfer system efficiency of 12.93%. The turn numbers are different in these two scenarios. Experiments were conducted to validate the optimization theory. Figure 16 also shows the experimental results which match well with the simulation. The discrepancies in results are due to the parasitic effects and AC resistance in the wire. In the experiment, the highest turn number was 40 since the self-inductance became too large for suitable matching capacitors. The harvested voltage reached maximum of 6.6 V at 15 turns as predicted. However, the power transfer system efficiency started to drop off after 30 turns from the peak of 13.61%. This is due to the increasing parasitic capacitance between the coil wires, as the spacing between wires became smaller when the turn number increased, which became more significant because the tuning capacitance became very small. Another reason is due to the H_z component distribution in the receiver plane at the 5-cm distance started to diverge and become a donut shape instead of a single peak when the coil spacing became smaller. This phenomenon caused the harvested energy to drop more than expected since the circuit theory did not consider this factor.

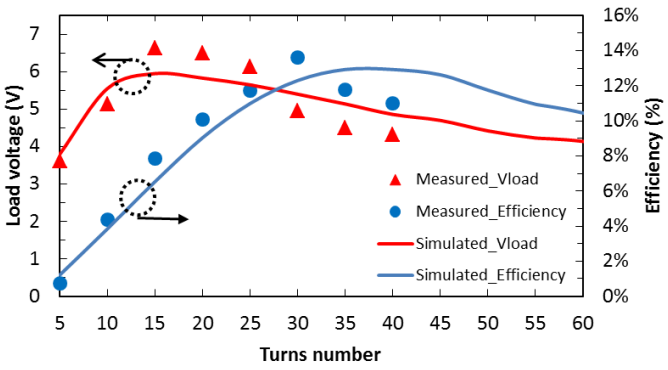

Figure 2-16 Simulated and measured load voltage and overall power transfer system efficiency as a function of transmitter coil turn number

In general, for wireless power transfer applications, system efficiency and transferred power amount should be considered simultaneously. For our targeted medical applications, however, the received voltage or power transfer amount have a higher priority than the efficiency as the implant needs sufficient energy to stimulate the tissues [4]. As the design strategy, for example, if the output power is required for 50 mW or 5 Vrms for the 500Ω load, the transmitter coil should range between 10 and 35 turns. A 35-turn transmitter coil would be preferred owing to a higher power transfer efficiency. However, the weight of the coil, which increases as the turn number increases, matching capacitance availability and parasitic effects may limit the turn number to a smaller one. These are the practical factors that need to be considered in the final design.

2.6 Conclusions

The field distributions of spiral coils in a wireless power transfer system have been examined theoretically and verified by both finite element simulations and experimental results. The wireless power system targeting medical applications, particularly gastrostimulatior, has significant difference in antenna sizes between the transmitter coil

worn outside the body and the receiver coil wrapped around the implant package inside the body. Thus, physical constraints exist, which require a trade-off consideration in design strategy. The field distribution studies help to plan for spatial and angular misalignment tolerances with respect to adaptive adjustment of the worn transmitter coil on patient's body. An optimization method of the spiral coil designs to obtain maximum power transfer or system efficiency was developed. The study in theory and experiments was conducted in the free space, thus future work will focus on investigation of the effect of human tissues utilizing our proposed design strategy.

Chapter 3

WIRELESS POWER TRANSFER FOR INDUSTRIAL APPLICATIONS

3.1 Introduction

Conventional single- input and single-output (SISO) systems which include one transmitter (TX) and one receiver antenna (RX) via close and mid-ranges have been examined in detail [38-43]. In such systems, the wireless power transfer and efficiency are limited by the antenna size and distance, since the electromagnetic fields decay exponentially when the transfer distance increases and diverge quickly when antenna size is small. Recent efforts to extend the transfer distance using a dipole coil resonant system (DCRS) with an optimal shaped ferrite core was developed showing enhancement in transfer efficiency over a distance of 5 m [44]. The power transferred between a single transmitter antenna and a single receiver antenna limits the number of electric devices in a system. Systems with single TX to power multiple RX or multiple TX to power single RX have been reported in [45-50]. In such systems, the power is transferred directly from TX to RX without the possibility for power redistribution or combining since the systems were not fully utilized either at the transmitter side or at the receiver side. The feasibility of scaling such systems to larger networks is also limited due to the electromagnetic field divergent of individual antennas. Therefore, the demand for a large scale wireless power system which can harvest powers from multiple sources and deliver powers to multiple users calls for a new system architecture.

In previous work, repeater antennas (RP) was used to combine the powers from two transmitters and deliver the powers to two receivers [51]. The RP has been used in a domino-resonator system and it plays an important role by introducing a low loss path for power to transfer indirectly instead of directly between TX and RX. This improves the overall wireless power transfer efficiency [52,53]. The prototype system [51] provides a

fundamental concept and quick implementation of a MIMO wireless power system. In this chapter, the technical issues of MIMO systems including coil misalignment effects, system bandwidths, power fluctuation due to loss of frequency synchronization is examined. The extension of the basic 2×2 network in [51] to a larger scale wireless power transfer system which can harvest powers from 4 TX to 6 RX is investigated.

3.2 System Model

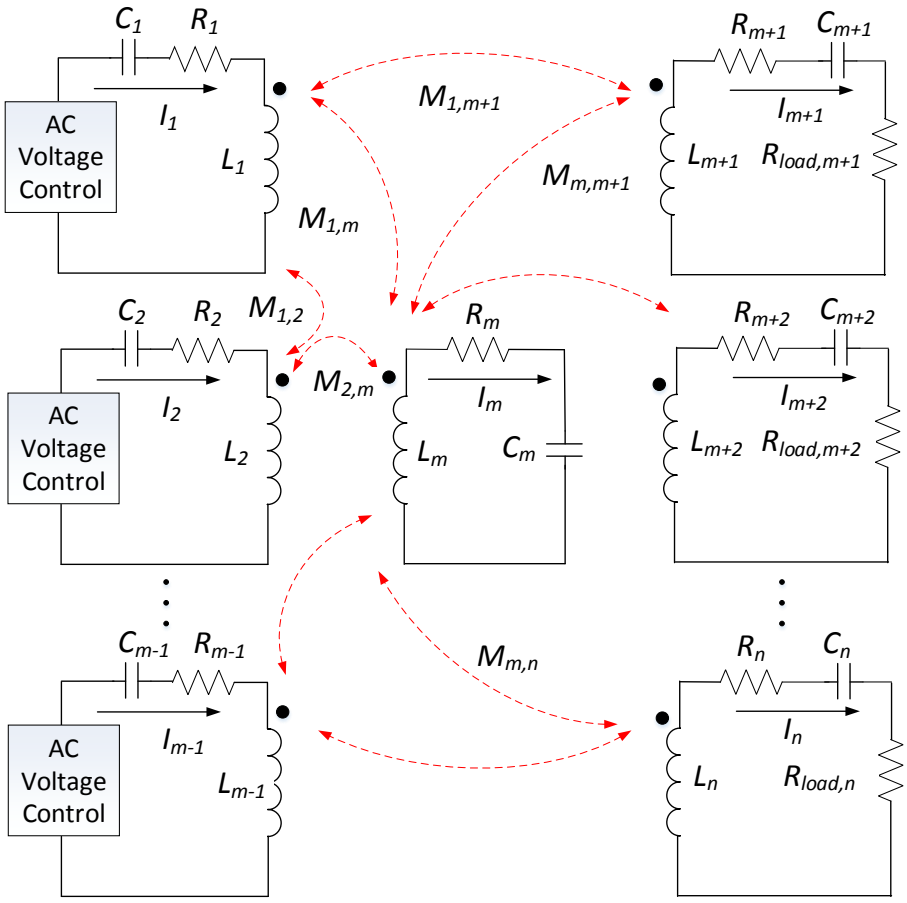

Figure 3-1 Lumped-element model for a wireless power system with multiple inputs and multiple outputs

The voltage equations for a MIMO wireless power system with a total of n antennas as shown in Fig. 3-1 can be expressed as an impedance matrix $\underline{Z}$ [56]:

$$\begin{bmatrix} Z_{1,1} & Z_{1,2} & \dots & Z_{1,n-1} & Z_{1,n} \\ Z_{2,1} & Z_{2,2} & \dots & Z_{2,n-1} & Z_{2,n} \\ \dots & \dots & \dots & \dots & \dots \\ Z_{i,1} & Z_{i,2} & \dots & Z_{i,n-1} & Z_{i,n} \\ \dots & \dots & \dots & \dots & \dots \\ Z_{n-1,1} & Z_{n-1,2} & \dots & Z_{n-1,n-1} & Z_{n-1,n} \\ Z_{n,1} & Z_{n,2} & \dots & Z_{n,n-1} & Z_{n,n} \end{bmatrix} \begin{bmatrix} I_1 \\ I_2 \\ \dots \\ I_i \\ \dots \\ I_{n-1} \\ I_n \end{bmatrix} = \begin{bmatrix} |V_1| \angle \phi_1 \\ |V_2| \angle \phi_2 \\ \dots \\ 0 \\ \dots \\ 0 \\ 0 \end{bmatrix} \tag{3.1}$$

where R_i, L_i and C_i are the resistance, inductance and compensation capacitance in the ith coil; R_{load} is the load resistance; M_{ij} is the mutual inductance between the ith and jth coils; ω is the angular frequency; $|V_i|$, θ_i, I_i are the voltage magnitude and phase, and current flowing in the ith coil, respectively. In Fig. 3-1, the TX include 1st coil to (m−1)th coil, the RP is mth coil and the RX include (m+1)th coil to nth coil.

In the $\underline{Z}$ matrix, the diagonal element $Z_{i,i}$ represents the series impedance of ith coil including coil resistance, inductance and compensation capacitance. Load resistances are included for impedances from $Z_{m+1,m+1}$ to $Z_{n,n}$. The off-diagonal element $Z_{i,j}=j\omega M_{ij}$ represents complex mutual impedances between coils. In the resonance condition ($\omega = 1/\sqrt{LC}$), the diagonal element $Z_{i,i}$ can be written as:

$$Z_{i,i} = R_i + j\left(\omega L_i - \frac{1}{\omega C_i}\right) = R_i \tag{3.2}$$

After obtaining the currents from Eq. 3.1, input power P_{input}, power delivered to the load P_{load}, power loss induced in all antennas P_{loss}, power transfer between antennas S_{ij} and the wireless power transfer efficiency $\eta_e\%$ can be calculated respectively as:

$$\begin{aligned} &P_{input} = Re\left\{\sum_{1\le i\le m-1} V_i \overset{*}{I}_i\right\};\quad P_{output} = \sum_{m+1\le i\le n} |I_i|^2 R_{load,i};\quad P_{loss} = \sum_{1\le i\le n} |I_i|^2 R_i \\ &S_{ij} = j\omega M_{ij} I_i \overset{*}{I}_j;\quad \eta_e\% = \frac{P_{output}}{P_{input}} \end{aligned} \tag{3.3}$$

3.3 Coil Misalignment Model

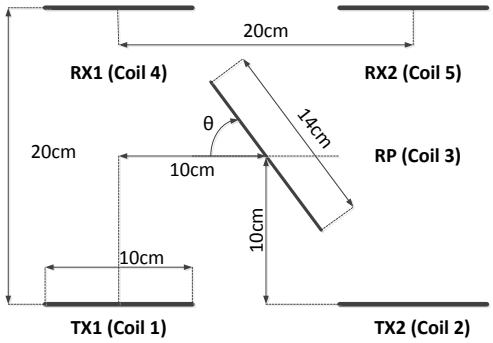

Figure 3-2 A MIMO wireless power system arrangement with two transmitter coils (TX_1, TX_2), two receiver coils (RX_1, RX_2) and a RP with a misalignment angle θ varied from 0^o to 180^o

Figure 3-2 [56] shows the arrangement of a MIMO system illustrating misalignment for the RP. Two transmitter and two receiver antennas are identical circular-shape coils with radii of 5 cm. Each pair of TX_1-RX_1 and TX_2-RX_2 is perfectly aligned in space. The RP is a 7-cm radius coil which can be rotated around its center position with a misalignment angle varying from 0^o to 180^o.

The mutual inductance between two misalignment coils shown in Fig. 3-3 can be calculated as [54]:

$$M = \frac{\mu_0}{\pi}\sqrt{R_P R_S}\int_0^{\pi}\frac{\left[\cos\theta - \frac{h}{R_S}\right]\Psi(k)}{\sqrt{V^3}}d\phi \tag{3.4}$$

with

$$V = \sqrt{1-\cos^2\theta\sin^2\theta - 2\frac{h}{R_S}\cos\phi\cos\theta + \frac{h^2}{R_S^2}};$$

$$\alpha = \frac{R_S}{R_P};\ \beta = \frac{c}{R_P};\ \gamma = \alpha - \beta\cos\phi\sin\theta;\ k^2 = \frac{4\alpha V}{(1+\alpha V)^2 + \gamma^2};$$

$$\Psi(k)=\left(\frac{2}{k}-k\right)K(k)-\frac{2}{k}E(k)$$

where R_P and R_S are the coil radii; c and h are the distances between centers and axes of coils; θ is the angle between the planes of coils; $K(k)$ and $E(k)$ are the complete elliptic integrals of the first and second kinds, respectively.

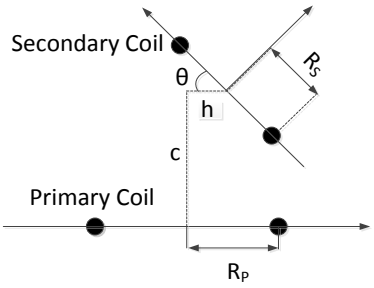

Figure 3-3 Top view of two filament circular loops with an angular misalignment at θ

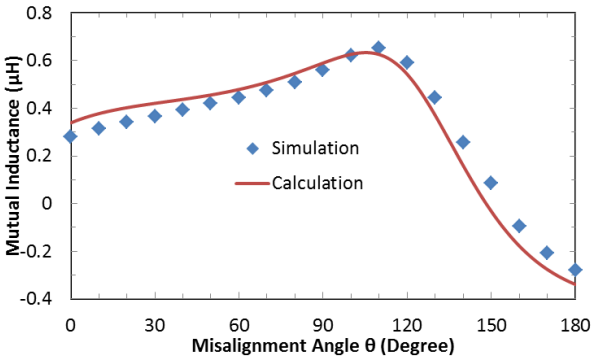

Figure 3-4 Mutual inductance between TX_1 and RP as a function of misalignment angle θ.

In a 2-coil system, j=1 and i=2 while the model can be utilized to calculate the mutual inductance between any two coils in a multiple coil system

The mutual inductance value can be extracted from the impedance parameters between the input and output ports as:

$$M_{ij}=\frac{Im(Z_{ij})}{2\pi f} \tag{3.5}$$

where $Im(Z_{ij})$ is the imaginary part of Z_{ij}.

Figure 3-4 [56] shows the calculated and simulated values of the mutual inductance between the TX_1 coil and RP coil when the misalignment θ varies from 0^o to 180^o. In a 2×2 system with one repeater as shown in Fig. 3-2, the mutual inductances between the RP coil and the other coils are related as:

$$\begin{aligned} M_{23}(\theta) &= M_{13}(180^o - \theta) \\ M_{34} &= M_{23} \\ M_{35} &= M_{13} \end{aligned} \tag{3.6}$$

owing to the symmetry of arrangement. The mutual inductances between any coil and the RP coil in this 2×2 system were found assuming the other coils were open loops. As observed, the mutual inductance starts to increase as θ increases, achieves a maximum and then decreases to a negative value at a certain angle since the sign of the voltage induced in the second coil depends on the relative directions of the windings in these two coils. The absolute value of M_{13} is maximized at 0.62 μH when θ is 110^o for the spatial arrangement in Fig. 3-2, resulting in a maximum flux linkage between the RP and TX_1 as well as between RP and RX_2. The power can thus be harvested from TX_1 to RP and then deliver to RX_2 with a higher efficiency. However, at 110^o between RP and TX_1, the mutual inductance value between the repeater coil RP and TX_2 as well as between the repeater coil RP and RX_1 can be obtained from Eq. 3.6 and Fig. 3-4 as:

$$M_{23}(110^o) = M_{13}(180^o - 110^o) = M_{13}(70^o) = 0.5\mu\text{H} \tag{7}$$

In this case, the RP coil will harvest less power from TX_2 than from TX_1 and deliver more power to RX_2 than to RX_1.

In a conventional wired power transmission system, power flow is controlled by changing voltage magnitudes and phases, thus the real and imaginary parts of powers to maintain a balanced condition between sources and loads. In a wireless power transfer

system, the relative angle between antennas, on the other hands, is an important parameter to control the powers harvested from transmitters and delivered to receivers since it determines the field coupling.

3.4 Experiments

The experimental setup with two TX, two RX and one RP coils were built to verify the coil misalignment model. High-efficiency class-E power amplifiers switched by a 5-V_{pp} square waveform at a duty circle of 50 % were used in the transmitter circuits to generate the carrier at 2 MHz. DC input power from the DC supply was fed into the Drain. The input DC voltage was fixed at 10 V at both transmitter circuits. Resistive loads of 30 Ω were connected in series in the receiver circuits to harvest the RF output power. DC input voltage and current from the power supply were measured to calculate input power while AC load voltages were measured to calculate the output power. The overall system efficiency η % was obtained as the ratio between the total output power delivered to two loads and the total input power from two TX. The overall system efficiency included the efficiency of the class-E amplifier η_{PA} % and the wireless efficiency η_e %, which can be calculated from Eq. 3-3:

$$\eta\% = \eta_{PA}\% \times \eta_e\% \tag{3.8}$$

Table 3-1 Coils Parameters

Coil	TX_1	TX_2	RP	RX_1	RX_1
Radius (cm)	5	5	7	5	5
Inductor (μH)	25	25	35	25	25
Resistor (Ω)	2	2	2.5	2	2
Load (Ω)	-	-	-	30	30
Turns number	10				
Materials	46 AWG/145 strands Litz wires				

The efficiency of the class-E amplifier was measured roughly at 90% after proper impedance matching, although the efficiency is expected to vary when the mutual inductance varies due to coil arrangement or distance changes. In each experiment, the amplifier impedance was tuned individually to ensure a maximum output. TX and RX coils were all identical as circular shapes with a 5-cm radius, while RP coil have a 7-cm radius. All coils were with 10 turns and made of 46AWG/146 strands Litz wires to reduce the skin and proximity effects at 2 MHz. Separate lumped capacitors were connected in series with each coil to tune each individual circuit at resonance. Coil parameters were summarized in Table 3-1. TX_1, RX_1 and RP were in clockwise winding direction while TX_2 and RX_2 were in counter clockwise winding direction. I reversed the winding direction of TX_2 and RX_2 in order to obtain $M_{13}=M_{23}$ at $\theta=90^o$. Therefore, magnetic field couplings from TX_1 and TX_2 to RP were constructive rather than destructive interference. System efficiency was measured with misalignment angle θ ranging from 0^o to 180^o by a step of 10^o. The phase shift between voltages at TX_1 and TX_2 was set to zero.

$$\phi=\phi_1-\phi_2=0^o \tag{3.9}$$

Figure 3-5 [56] shows the measured overall system efficiency as a function of angle θ varying from 0^o to 180^o. As observed, a maximum efficiency of 45.09% can be achieved at $\theta=90^o$. In this case, the RP coil is orthogonal to all TX and RX coils. When $\theta=0$, as the RP coil is parallel to the other coils, the efficiency is reduced to a minimum of 1.68%. When the RP coil is removed, the efficiency from the 2 transmitters to 2 receivers without a RP is also at 1.68%.

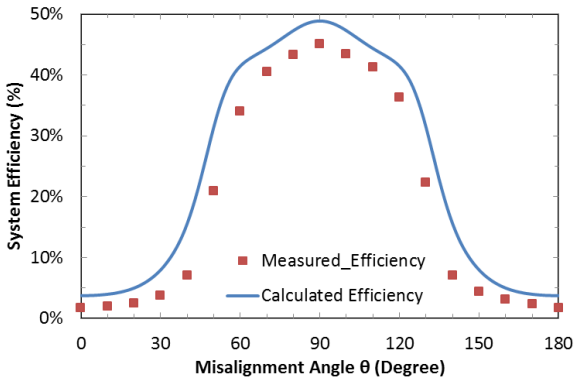

Figure 3-5 System efficiency as a function of misalignment angle θ

The power flow diagrams for 4 different values of θ at 0°, 30°, 60° and 90° were calculated and presented in Fig. 3-6 [56]. At 0°, M_{13} was 0.34 µH while M_{23} was −0.34 µH, as shown in Table 3-2. In this case, the induced current in the RP coil was zero since the flux linkages between TX_1-RP and TX_2-RP cancelled each other since the mutual inductance was in the opposite signs. Since no current induced in the RP, the power was transferred directly from TX to RX with an overall efficiency of only 1.68%. No power was transferred directly between TX_1 and TX_2 as well as between RX_1 and RX_2 since I_1, I_4 and I_2, I_5 are in phase, respectively. When θ increased to 30°, more power from TX_1 was transferred to the repeater as M_{13} increased to 0.42 µH. However, part of the power was transferred back from the repeater to TX_2, and thus the efficiency was low at 3.74% due to the high loss induced in the RP. In addition, 3.45 W was exchanged directly between TX_1 and TX_2, and 0.05 W was exchanged directly between RX_1 and RX_2 because power flow was unbalanced. When θ increased to 60°, M_{13} and M_{23} were higher and the efficiency increased to 34.07%. At 90°, the efficiency was maximized at 45.09% and the system was in a balance condition since the power flows were symmetric.

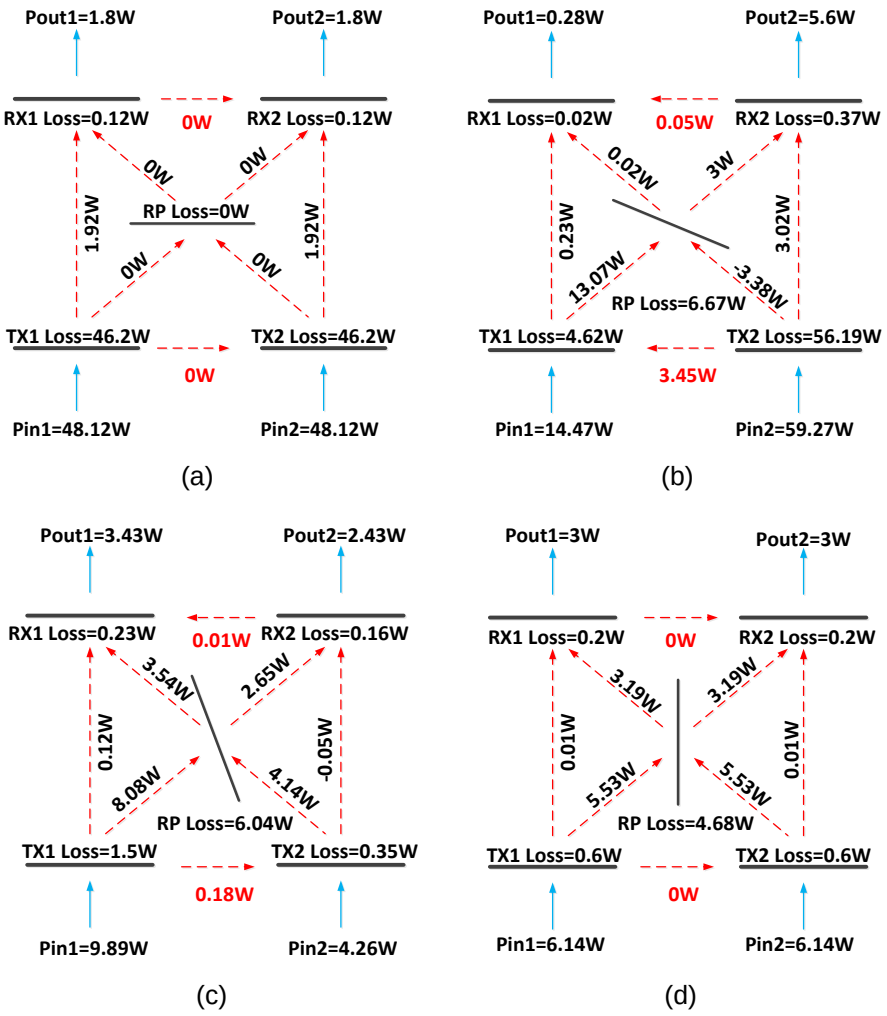

Figure 3-6 Calculated power flow diagrams of the 2×2 MIMO system at 4 different misalignment angle θ of (a) 0°, (b) 30°, (c) 60° and (d) 90°. The configurations are illustrated in top views of the coil arrangements

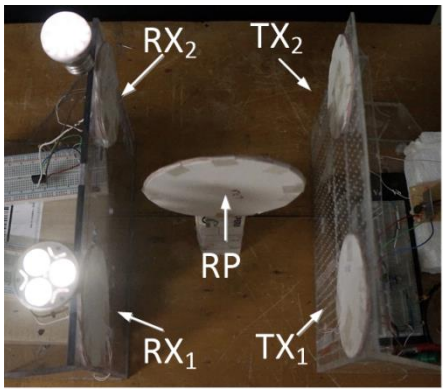

Figure 3-7 Demonstration of a 2×2 MIMO wireless power system utilizing a RP to harvests the power from two TX and deliver the power to light up two 3-W LED bulbs with an overall system efficiency of 45%

Experimental demonstration for the 2×2 MIMO system was shown in Fig. 3-7 [56]. In this setup, 30-Ω load resistors in the receivers were replaced by 3-W LED bulbs for demonstration. Full wave bridge rectifiers were utilized in the receiver circuits to power the LEDs. The misalignment angle θ was set at 90^{o} since the RP coil was orthogonal to $TX_{1,2}$ and $RX_{1,2}$. The input power was increased and recorded to be 13.4 W at the time when the LEDs were turned on. The total efficiency was measured at 45%.

The system performance of the 2×2 system due to load variations is examined and the result is shown in Fig. 3-8 [56]. In general, load resistance and inductance can vary in practical conditions. Since inductance can be compensated by proper matching capacitors, only resistance variations is needed to verify. The system efficiency was measured as the load resistances in both receivers increased from 5 to 100 Ω in steps of 5 Ω. A maximum efficiency was obtained at 20 Ω. The system maintained the transfer efficiency above 45% within the load ranging from 10 to 35 Ω. The efficiency dropped below 30% as the load resistance reached 60 Ω.

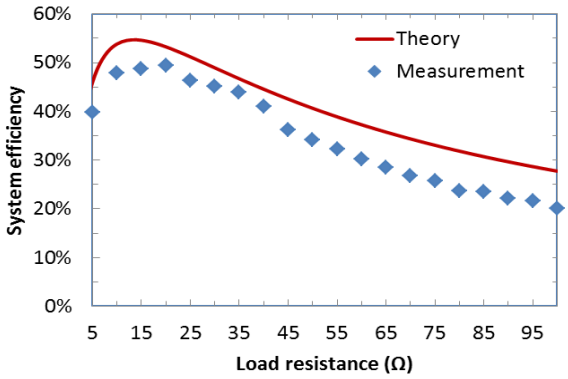

Figure 3-8 System efficiency as a function of load from 5 to 100 Ω

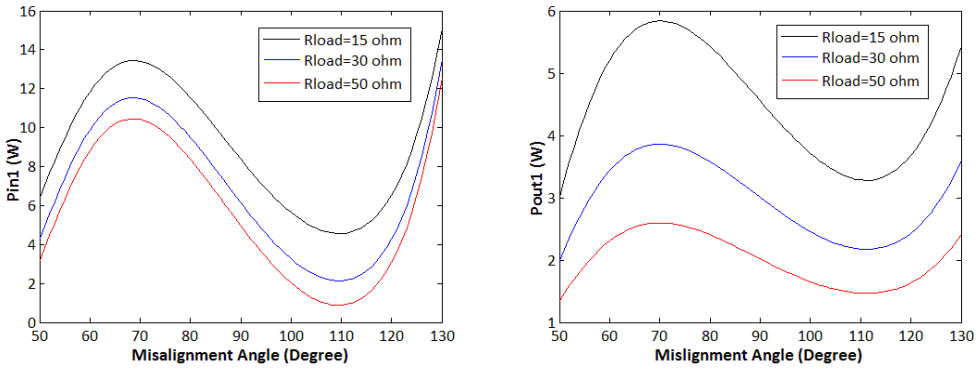

(a) (b)

Figure 3-9 Variation of (a) input power fed into TX1 and (b) output power received at RX1 with respect to the misalignment angle θ at different values of load resistance

Table 3-2 Power Loss and System Efficiency

θ	M_{13} (μH)	M_{23} (μH)	TX Loss	M_{12} (μH)	M_{14} (μH)	M_{15} (μH)	RP Loss	RX Loss	System Efficiency	
									Calculated	Measured
0°	0.34	-0.34	96.0%	0.09	0.13	-0.02	0	0.3%	3.8%	1.7%
30°	0.42	-0.03	86.6%				7.6%	0.4%	7.9%	3.7%
60°	0.48	0.54	13.8%				42.4%	2.7%	41.4%	34.1%
90°	0.59	0.59	9.7%				38.1%	3.3%	48.8%	45.1%

Input and output power variations due to the change of load resistance were also examined in Fig. 3-9 [56]. Since the system arrangement was symmetric, only Pin1 and Pout1 were presented. Both input power and output power decreased as the load resistance increased from 15 Ω to 50 Ω. However, the output power decreased with a higher rate than the input power, resulting in further decrements of the system efficiency. This was also expected from the results in Fig. 3-8 since the system efficiency was maximized at 15 Ω.

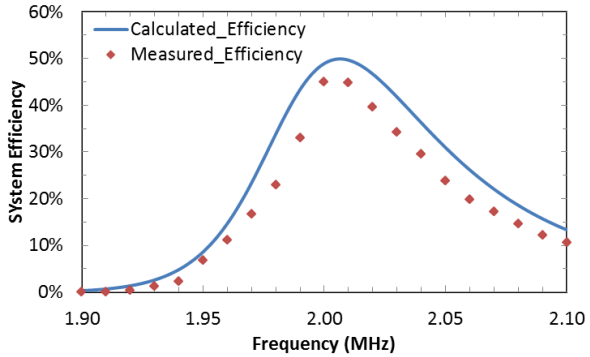

Figure 3-10 System efficiency as a function of frequency at θ=90°

System performance due to frequency variations when θ was 90° was measured and compared with theory in Fig. 3-10 [56]. All coils were individually tuned into resonance at 2 MHz and the system efficiency was measured from 1.9 MHz to 2.1 MHz by a step of 10 kHz. During frequency variations, the coils were not tuned for each individual frequency. The maximum calculated efficiency of 49.92% was achieved at 2.006 MHz. At 2 MHz, the calculated efficiency was 48.86%. The ratio between the optimum frequency, at which the maximum efficiency occurred, and the resonance frequency was f_{opt}/f_{res} = 1.003 in this case. This off-resonance phenomenon due to the cross coupling effect between TX and RX has been examined in [52]. System efficiency could be maintained above 33% with a

40-kHz frequency variation from 1.99 to 2.03 MHz and dropped to below 10% as the frequency was out of the 1.96 to 2.1 MHz range.

3.5 Power Fluctuation due to Loss of Frequency Synchronization

In general, a wireless power transfer system operates at the resonance frequency when all transmitter coils are excited by synchronized sources. However, due to the loss of frequency synchronization which could occur as transmitters are located at different places or driven by different sources (Fig. 3-11) [56], the relative phase between voltage sources is no longer constant but varying in time, which causes voltage magnitude instability and power oscillation. The power flows of the entire system during loss of synchronization can be analyzed by using the superposition method assuming the power distribution is a linear system.

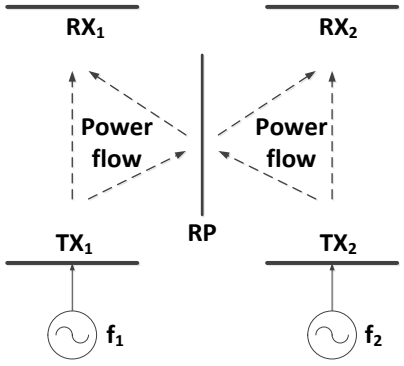

Figure 3-11 2-input and 2-output wireless power system which transmitters were excited by different frequencies. The coil arrangement is in top view

Assuming TX_1 is excited at a frequency of f_1 while TX_2 at f_2, the frequency "slip" is defined as:

$$f_{slip} = f_2 - f_1 > 0 \tag{3.10}$$

The phase shift at a time period Δt after the loss of synchronization can be expressed as:

$$\Delta\phi = 2\pi f_{slip}\Delta t \tag{3.11}$$

The load voltages in receiver coils are superposed as:

$$\begin{aligned} V_{load1} &= V_{load1}(f_1) + V_{load1}(f_2) \\ V_{load2} &= V_{load2}(f_1) + V_{load2}(f_2) \end{aligned} \tag{3.12}$$

At the initial condition, the phase shift is set to zero and two components are in phase. After a time period Δt, since $f_2 > f_1$, the f_2 component is ahead of the f_1 component in phase and the phase shift accumulates to $\Delta\phi=2\pi f_{slip}\Delta t$. When $\Delta\phi=180^o$, f_1 and f_2 components are out of phase and cancel each other. However, since the magnitudes of f_1 and f_2 components are not equal, the load voltage magnitude will not become zero at $\Delta\phi=180^o$.

Fig. 3-12 [56] shows the measured load voltage waveforms which were captured from a digital oscilloscope. The top curve was the load voltage in RX_1 while the bottom one was for RX_2. In this setup, the RP was 90° with respect to the TX and RX. The waveforms were captured in three different cases: (a) when TX_1 and TX_2 were both excited by 2 MHz; (b) when TX_1 was excited by 1.975 MHz and TX_2 at 2.025 MHz; (c) when TX_1 was excited by 1.95 MHz while TX_2 was at 2.05 MHz. The recording duration was 20 µs. When the frequencies were synchronized, the load voltage waveforms were stable and the amplitudes were at maximum, as expected. However, when f_{slip} increased to 50 kHz the waveforms were no longer stable and started to fluctuate within few cycles as shown in Fig. 3-12(b). The amplitude also decreased by 50% as the system was off-resonance. The waveform patterns of V_{load1} and V_{load2} were not similar since RX_1 received most of the power from both RP and TX_1 while RX_2 received power mostly from both RP and TX_2. The rms (root mean square) voltage value was obtained from the waveforms to calculate the load

power. The average power delivered to RX_1 was 234 mW with a variation of 265 mW over the beat frequency of 50 kHz. The average power delivered to RX_2 was 155 mW with a 295-mW variation over the beat frequency of 50 kHz. When f_{slip} increased to 100 kHz the voltage fluctuation became more severe and the amplitude was further decreased as in Fig. 3-12(c). The average power delivered to RX_1 now was 79 mW with a variation of 145 mW over the beat frequency of 100 kHz while the average power delivered to RX_2 was 52 mW with a 35-mW variation over the same beat frequency. The power fluctuations under misalignment are also examined and the results are shown in Fig. 3-13 [56]. In this setup, the RP was 45° with respect to the TX and RX. Similar to the results in Fig. 3-12, the waveforms were stable and at maximum when synchronized. Voltage fluctuations became a major issue when f_{slip} increased to 50 kHz and 100 kHz. When frequencies were synchronized, the load voltage at RX_1 was higher than RX_2 due to unbalance power flow resulting from misalignment.

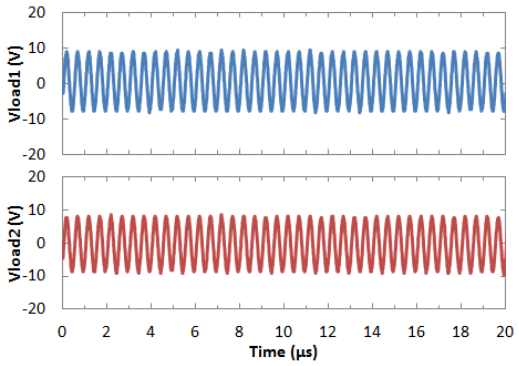

(a)

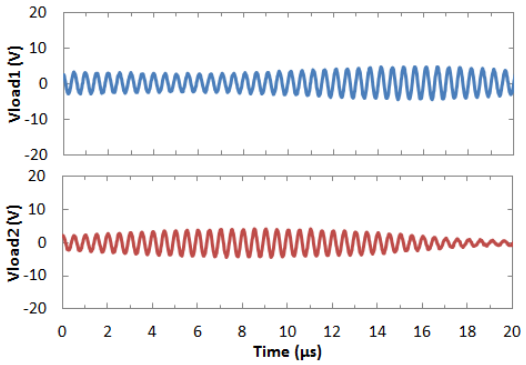

(b)

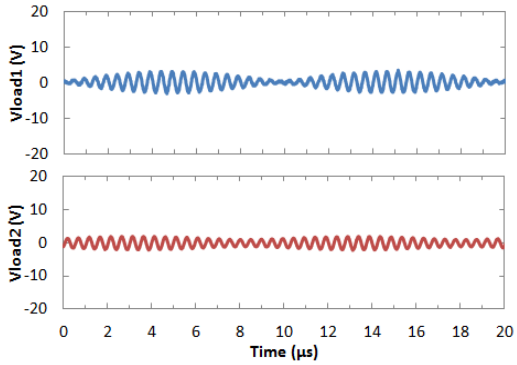

(c)

Figure 3-12 Measured load voltage waveforms for (a) synchronized sources

(b) f_{slip}=50 kHz and (c) f_{slip}=100 kHz cases with a recording time of 20 μs

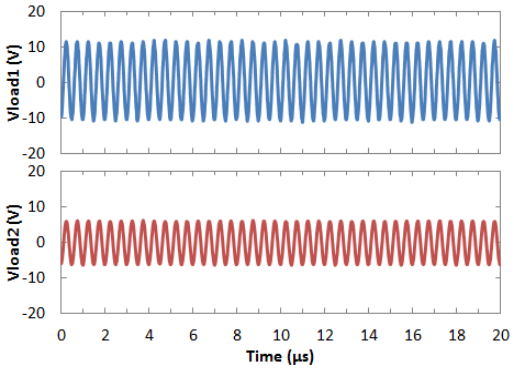

(a)

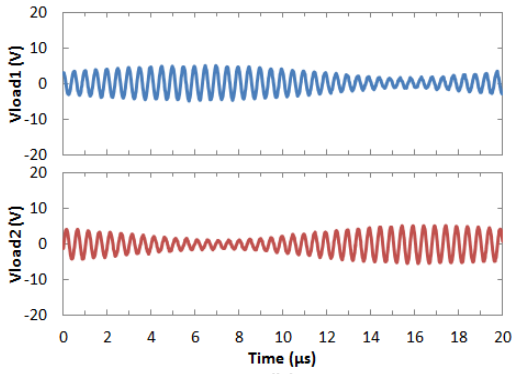

(b)

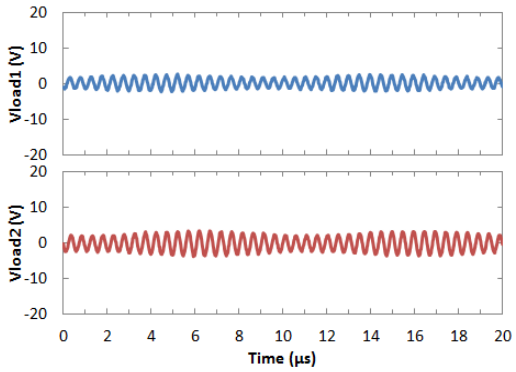

(c)

Figure 3-13 Measured load voltage waveforms for (a) synchronized sources, (b) f_{slip}=50 kHz and (c) f_{slip}=100 kHz cases with a recording time of 20 µs. The RP was 45^{o} with respect to the TX and RX

3.6 Scaling the Wireless Power Transfer System

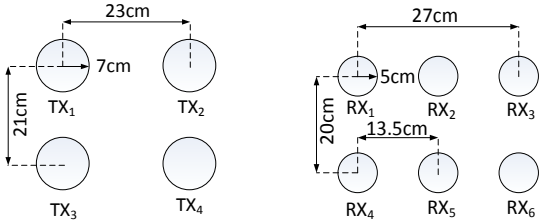

(a) (b)

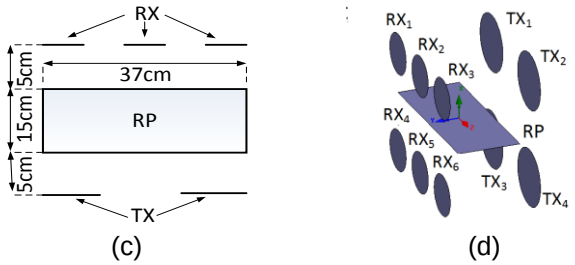

(c) (d)

Figure 3-14 A 4-input and 6-output wireless power transfer system arrangement. (a) TX array. (b) RX array. (c) Top view and (d) 3D view of the system

Similar system architecture and mathematical model can be extended to a larger scale of multi-input multi-output system which may be of interest for power combining and distribution. In a power-grid-like configuration, power fluctuation due to load add-drop and synchronization variation is critical for system stability. In the following experiment, the 2×2 prototype network is extent to a larger scale system which harvested powers from 4 TX to 6 RX, as shown in Fig. 3-14 [56]. In this demonstration, TX and RX were circular coils with radii of 7 cm and 5 cm, respectively. The system is designed with more RX than TX with a consideration that in a power grid the number of loads was generally larger than the number of sources. The size of TX coils was designed to be bigger as they usually need to handle more power than RX coils. A rectangular-shape coil was utilized as the repeater coil in order to spatially accommodate all TX and RX. Coil parameters including measured AC resistances, self-inductances are given in Table 3-3. The mutual inductances between each pair of TX, RX and RP were given in Table 3-4. Similar to the 2×2 system, the winding directions of $TX_{3,4}$ and $RX_{4,5,6}$ are reversed so that the mutual inductances between the RP and all the remaining coils have the same sign. The carrier frequency driving the transmitter amplifiers was set at 2 MHz. The DC input voltage and current to the class-E amplifier were measured to calculate the input power. The load rms voltages were used to calculate the

output power. The system efficiency $\eta\%$ was measured as the ratio between the total output power delivered to 6 receivers and the total DC input power fed into 4 transmitters.

Table 3-3 Coil Parameters

Coil	TX	RP	RX
Resistance (Ω)	2.5	9	2
Inductance (μH)	35	145	25
Size	5cm radius	15cm × 37cm	7cm radius
Material	46 AWG/145 strands Litz wires		

Table 3-4 Mutual Inductance (μH) Between Coils in 4×6 System

	TX_1	TX_2	TX_3	TX_4	RP	RX_1	RX_2	RX_3	RX_4	RX_5	RX_6
TX_1	-	-0.253	-0.352	-0.091	1.405	0.129	0.081	0.015	0.031	0.023	0.003
TX_2	-0.253	-	-0.091	-0.352	1.405	0.015	0.081	0.129	0.003	0.023	0.031
TX_3	-0.352	-0.091	-	-0.253	1.405	0.031	0.023	0.003	0.129	0.081	0.015
TX_4	-0.091	-0.352	-0.253	-	1.405	0.003	0.023	0.031	0.015	0.081	0.134
RP	1.405	1.405	1.405	1.405	-	0.692	0.894	0.692	0.692	0.894	0.692
RX_1	0.129	0.015	0.031	0.003	0.692	-	-0.384	-0.034	-0.091	-0.049	-0.017
RX_2	0.081	0.081	0.023	0.023	0.894	-0.384	-	-0.384	-0.049	-0.091	-0.049
RX_3	0.015	0.129	0.003	0.031	0.692	-0.034	-0.384	-	-0.017	-0.049	-0.091
RX_4	0.031	0.003	0.129	0.015	0.692	-0.091	-0.049	-0.017	-	-0.369	-0.034
RX_5	0.023	0.023	0.081	0.081	0.894	-0.049	-0.091	-0.049	-0.369	-	-0.369
RX_6	0.003	0.031	0.015	0.134	0.692	-0.017	-0.049	-0.091	-0.034	-0.369	-

Table 3-5 Power Flow and Loss Allocation in the 4×6 System

Power flow	Full system	TX_1 off	TX_2 off	RX_1 off	RX_2 off	RX_3 off
$P_{TX1\text{-}RP}$	8.79W	0	10.04W	8.52W	8.07W	8.02W
$P_{TX2\text{-}RP}$	8.79W	10.04W	0	8.02W	8.07W	8.52W
$P_{TX3\text{-}RP}$	8.79W	10.04W	13.93W	9.35W	8.45W	7.96W
$P_{TX4\text{-}RP}$	8.79W	13.93W	10.04W	7.96W	8.45W	9.35W
$P_{RP\text{-}RX1}$	3.05W	3.02W	2.88W	0	3.54W	3.25W
$P_{RP\text{-}RX2}$	4.96W	4.81W	4.81W	5.42W	0	5.42W
$P_{RP\text{-}RX3}$	3.05W	2.88W	3.02W	3.25W	3..54W	0
$P_{RP\text{-}RX4}$	3.05W	3.05W	2.84W	3.25W	3.33W	3.16W
$P_{RP\text{-}RX5}$	4.96W	4.79W	4.79W	5.22W	5.42W	5.22W
$P_{RP\text{-}RX6}$	3.05W	2.84W	3.05W	3.16W	3.33W	3.25W
TXloss	4.88%	7.08%	7.08%	4.61%	4.29%	4.61%
RPloss	35.03%	34.19%	34.19%	37.95%	40.03%	37.95%
RXloss	3.76%	3.67%	3.67%	3.59%	3.48%	3.59%
Calculated $\eta\%$	56.33%	55.06%	55.06%	53.86%	52.23%	53.86%
Measured $\eta\%$	54.72%	51.32%	50.74%	49.02%	47.91%	48.14%

In the experiment for the 4×6 system, each coil is tuned by compensation capacitors to resonance at 2 MHz. The experiment is started with the full system setup in which the efficiency was measured at 54.7%. The power delivered to RX_2 and RX_5 was 4.96 W each which was higher than 3.05 W delivered to RX_1, RX_3, RX_4, or RX_6. This is due to that RX_2 and RX_5 were in the center position of RP and have a higher mutual inductance with RP, as shown in Table 3-4. Practical applications may require the system to operate in high efficiency during network variation. The variation may range from small disturbances such as single source or load switching on or off, to large disturbances such as adding or dropping multiple loads or changing power transfer routing configuration. Within the scope of this research, the system performance under small disturbances is examined: when one TX (TX_1 or TX_2) was disconnected; or when one RX (RX_1, RX_2 or RX_3) was disconnected from the network. The power flow data are shown in Table 3-5. When one TX was disconnected, the other 3 TXs need to send more power to the RP to keep up with the required load. The system efficiency slightly decreased from 54.7% to 51.3% due to the burden of more power from TX creating more ohmic losses in the TX. When one RX was disconnected, the system efficiency decreased to the range between 49% and 47.9%. The power transfer between TX-TX and RX-RX was zero when all coils were presented due to the power flow symmetry, which was similar to the 2×2 system. When one TX or one RX was disconnected, the system arrangement was no longer symmetric and then power exchanged between TX-TX and RX-RX. The maximum power transfer between TX-TX and RX-RX were 0.64 W and 0.01 W, which accounted for 1.7% and 0.03% of the total input power, respectively. These exchanged powers were relatively small and could be ignored under a small disturbance condition. In general, the system can maintain a high

efficiency of about 50% when one coil was disconnected from the grid. This result demonstrated the ability of the system to tolerate the small disturbance from dynamic source and load variations.

In a linear system no nonlinear insertion losses, when the input powers increase, the power flows and output powers also scale at the same rate and system efficiency remains the same. When network configuration changes, on the other hands, the power flows will change. The change in the power flows results in the change of system efficiency.

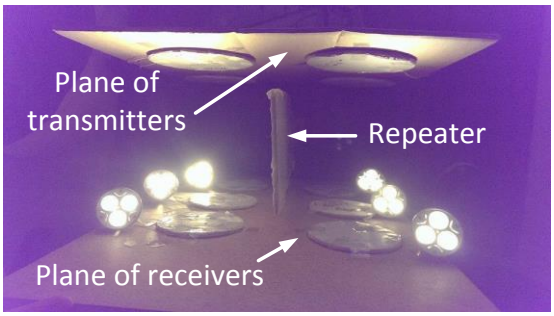

Figure 3-15 Demonstration of a 4-input and 6-output wireless power transfer system which harvests the powers from four TX and delivers the powers to light up six 3-W LED bulbs. The photo is showing the top view. The overall system efficiency was measured at 50%

Experimental demonstration for the 4×6 MIMO system is shown in Fig. 3-15 [56]. Similarity to the 2×2 MIMO system in Fig. 3-7, the load resistors were replaced by 3-W LED bulbs. The input powers from all TX were recorded at 42 W at the time when all the LED bulbs were turned on. The overall system efficiency was measured at 50%. The demonstrated 2×2 and 4×6 systems can be extended to a larger m×n system by increasing the size of the repeater antenna to spatially cover all TX and RX antennas. However, the AC resistance of the RP might become significant and induce outstanding ohmic losses affecting the overall system performance. As observed in Tables 3-2 and 3-5, the RP

losses were accounted for more than 30% in both 2×2 and 4×6 systems. Therefore, the size of RP becomes a major limitation to implement large scale systems. A possible remedy is to modify the network architecture by dividing a large RP into multiple smaller repeaters. Each smaller RP will only need to handle smaller amounts of power, hence, reduce power losses. Small RP can be arranged to spatially accommodate all TX and RX allowing more efficient ways for physical arrangement. In such systems, the 2×2 arrangement is the building block for a larger network. Of course, it is obvious that the size, number and position of RP, and coil designs need to be optimized to achieve maximum efficiencies for different power and physical requirements in specific applications. Similar studies to our investigation method can be applied for the targeted designs.

3.7 Conclusions

A wireless power transfer network architecture which can harvest powers from multiple transmitters (TX) and deliver the powers to multiple receivers (RX) is demonstrated. The system performance has been examined by theory and verified by experimental setups of 2×2 and 4×6 systems. The power transfer and system efficiency can be significantly enhanced by utilizing a RP coil. The coil orientation is an important factor as it varies the power flows from TX to RX. The results from a scaled system with 4 TX and 6 RX show that the system can operate at a sufficient efficiency when the source or load dynamically drops out of the grid. These demonstrations show feasibility for future implementation of large-scale electrical power combining and distribution in the free space and possible applications utilizing management of dynamic power flows. Future wireless power systems may incorporate optimal designs of RP to control the power flows adaptively in order to maintain the system at maximum efficiency.

Chapter 4

FREQUENCY MODES IN WIRELESS POWER TRANSFER SYSTEM

4.1 Introductions

In conventional near-field and far-field theories, power transfer and system efficiency attenuate at the rate of d^3 where d is the transfer distance between transmitter and receiver. However, recent studies show that there exists an over-coupled region where maximum transfer power can be maintained at constant [65-69]. In this region, the resonant frequency is split into the low- and high-mode ones. As the transfer distance increases beyond a critical distance, these two frequency modes converge into the self-resonance frequency of the system. Several works reported the frequency splitting phenomenon in systems with multiple TXs or multiple RXs [45-49,70]. In such systems, the power is transferred directly from single TX to multiple RXs or from multiple TXs to single RX. However, it still lacks investigation in systems implementing diversity on both TX and RX sides.

In [56], a new system architecture which can harvest the power from multiple TXs and deliver/distribute the electromagnetic power to multiple RXs simultaneously was introduced. In such multi-input multi-output (MIMO) systems, a repeater is used to create strong coupling between TXs and RXs, and to enhance the transfer efficiency significantly. The MIMO systems show great advantages in controlling the power flow between antennas and are capable of maintaining system stability under load-disturbance conditions such as one TX or one RX is disconnected from the distribution network [56]. In this research, the frequency splitting phenomena in the MIMO wireless power transfer system is examined. Analytical model based on eigenvalue analysis is used to predict the frequency modes. These frequency modes are validated by an experimental setup with two TX, two RX and one repeater.

4.2 System Model

4.2.1 Single-Input and Single-Output WPT System

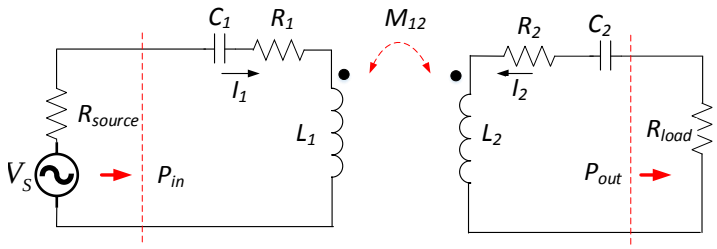

Figure 4-1 Equivalent circuit of the SISO WPT system

Figure 4-1 [75] shows the equivalent circuit of the conventional single-input and single-output wireless power transfer system. The impedance matrix of the system is represented as:

$$\underline{Z} = \begin{bmatrix} Z_{11} & Z_{12} \\ Z_{21} & Z_{22} \end{bmatrix} \tag{4.1}$$

where $Z_{11}=R_1+i(\omega L_1-1/\omega C_1)$, $Z_{22}=R_2+i(\omega L_2-1/\omega C_2)$ and $Z_{12}=Z_{21}=i\omega M_{12}$; M_{12} is the mutual inductance between TX and RX; ω is the angular frequency of the system; R_1, L_1, C_1 and R_2, L_2, C_2 are the series resistance, inductance and matching capacitance of the TX and RX, respectively. The desired resonant frequency is determined as: $\omega_0 = 1/\sqrt{L_1C_1} = 1/\sqrt{L_2C_2}$ which is indicated as the center frequency.

The scattering matrix $\underline{S}$ is related to the impedance matrix $\underline{Z}$ by:

$$\underline{S} = \left(\underline{Z} - Z_0\underline{U}\right)\left(\underline{Z} + Z_0\underline{U}\right)^{-1} \tag{4.2}$$

where Z_0 is the reference impedance; $\underline{U}$ is the identity matrix which has the same dimension as $\underline{Z}$.

If the source and load impedance match with the reference impedance, the normalized transfer power (P_{norm}) and the transfer efficiency (η) can be simplified as:

$$P_{norm} = \frac{P_{out}}{P_{in\_\max}} = \left|S_{21}\right|^2 \tag{4.3}$$

$$\eta = \frac{P_{out}}{P_{in}} = \frac{\left|S_{21}\right|^2}{1-\left|S_{11}\right|^2} \tag{4.4}$$

where P_{in_max} is the maximum input power delivered from the source and is obtained from the Thevenin's theorem as:

$$P_{in\_\max} = \frac{\left|V_S\right|^2}{8R_{source}} \tag{4.5}$$

System parameters of the SISO system are given in Table 4-1. Normalized transfer power and transfer efficiency variation versus normalized frequency and coupling coefficient are related and shown in Figs. 4-2 and 4-3 [75], respectively. Normalized frequency is determined as the ratio between the actual frequency and the center frequency. As seen from the plots, the frequency splitting is only observed in the normalized transfer power while the transfer efficiency is always maximum at the center frequency. The main difference between these two plots is that the transfer efficiency takes into account the variation of the input power due to strong coupling while the transferred output power varies. The strong mutual coupling from the RX affects the equivalent impedance seen from the input side and coordinately varies the input current in the TX. Therefore, transfer power and transfer efficiency are not necessarily maximized at the same time.

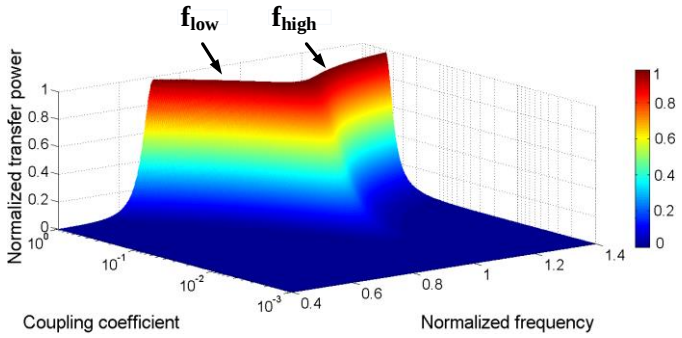

Figure 4-2 Normalized transfer power as a function of coupling coefficient and normalized frequency in the SISO system

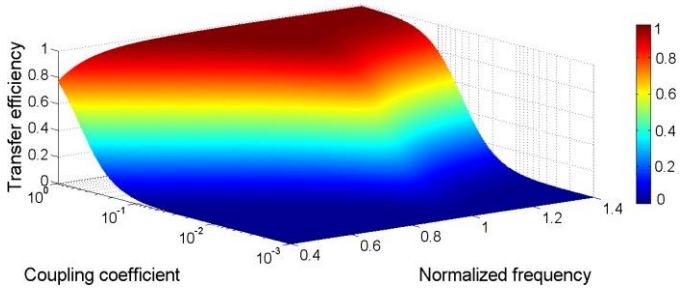

Figure 4-3 Transfer efficiency as a function of coupling coefficient and normalized frequency in the SISO system

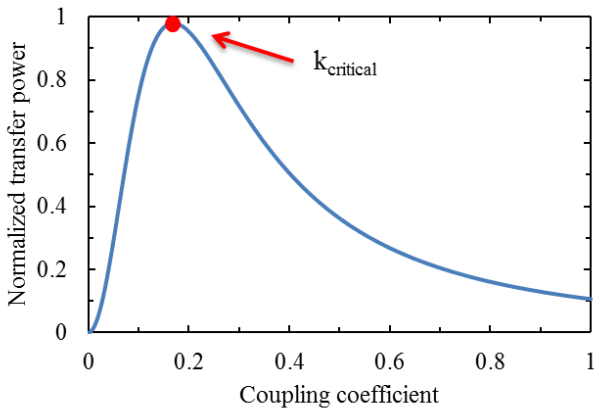

Figure 4-4 Normalized transfer power at the operating (center) frequency in the SISO system

Table 4-1 SISO System Parameters

Parameter	Value
R_{source}	50 Ω
R_{load}	50 Ω
Z_0	50 Ω
L_1,L_2	7 μH
C_1,C_2	78.7 pF
R_1,R_2	0.5 Ω

Figure 4-4 [75] shows the variation of normalized transfer power versus the coupling coefficient at the center frequency. The transfer power is maximized at the critical coupling coefficient $k_{critical}$. At the over-coupled region ($k>k_{critical}$), the system resonant frequency is split into low and high modes, which leads to a low transfer power at the operating (center) frequency. The over-coupled region is typically at a near distance. At the under-coupled region ($k<k_{critical}$), the transfer power attenuates quickly as the coupling coefficient decreases which usually means the transfer distance increases. The critical coupling coefficient can be obtained by taking the differential of the output power and setting it equal to zero.

The output power at the center frequency is calculated from the equivalent circuit as [69]:

$$P_{out}\,|_{\omega=\omega_0} = \frac{\omega_0^2 k^2 L_1 L_2 V_S^2 R_{load}}{\left[\left(R_{source}+R_1\right)\left(R_{load}+R_2\right)+\omega_0^2 k^2 L_1 L_2\right]^2} \tag{4.6}$$

$$\frac{\partial P_{out}}{\partial k}\,|_{\omega=\omega_0} = 0 \leftrightarrow k_{critical} = 1/\sqrt{Q_1 Q_2} \tag{4.7}$$

where Q_1 and Q_2 are the quality factors of TX and RX, respectively.

The low- and high-mode frequencies can be calculated using the eigenvalue analysis [71,72]. The impedance matrix equation under no excitation condition is:

$$\begin{bmatrix} R_1+R_{source}+i\omega L_1+\dfrac{1}{i\omega C_1} & i\omega M \\ i\omega M & R_2+R_{load}+i\omega L_2+\dfrac{1}{i\omega C_2} \end{bmatrix} \begin{bmatrix} I_1 \\ I_2 \end{bmatrix} = \begin{bmatrix} 0 \\ 0 \end{bmatrix} \tag{4.8}$$

Divide the 1st row by $i\omega L_1$ and 2nd row by $i\omega L_2$, we get:

$$\begin{bmatrix} \frac{R_1 + R_{source}}{i\omega L_1} + 1 - \frac{\omega_0^2}{\omega^2} & k_{12}\sqrt{L_2 / L_1} \\ k_{12}\sqrt{L_1 / L_2} & \frac{R_2 + R_{load}}{i\omega L_2} + 1 - \frac{\omega_0^2}{\omega^2} \end{bmatrix} \begin{bmatrix} I_1 \\ I_2 \end{bmatrix} = \begin{bmatrix} 0 \\ 0 \end{bmatrix} \tag{4.9}$$

Or

$$\begin{bmatrix} \frac{1}{iQ_1} + 1 & k_{12}\sqrt{L_2 / L_1} \\ k_{12}\sqrt{L_1 / L_2} & \frac{1}{iQ_2} + 1 \end{bmatrix} \begin{bmatrix} I_1 \\ I_2 \end{bmatrix} = \frac{\omega_0^2}{\omega^2} \begin{bmatrix} I_1 \\ I_2 \end{bmatrix} \tag{4.10}$$

Assumed all coils have high quality factors, the term $1/iQ_i$ can be neglected from the diagonal elements, the equation is simplified as:

$$\underline{A}\underline{I} = \lambda \underline{I} \tag{4.11}$$

where $$\underline{A} = \begin{bmatrix} 1 & k_{12}\sqrt{L_2 / L_1} \\ k_{12}\sqrt{L_1 / L_2} & 1 \end{bmatrix}$$

$\underline{I}$ is the eigenvector and $\lambda = \omega_0^2/\omega^2$ is the eigenvalue of the matrix $\underline{A}$, which can be calculated from:

$$\det\left|\underline{A} - \lambda \underline{U}\right| = 0 \tag{4.12}$$

where $\underline{U}$ is the identity matrix.

Solving Eq. 4-12, we obtain two solutions:

$$\lambda = 1 \pm k_{12} \text{ or } \frac{\omega_0^2}{\omega^2} = 1 \pm k_{12} \tag{4.13}$$

The low-mode and high-mode frequencies are obtained from Eq. 4-13 as:

$$\begin{aligned} \omega_{low} &= \frac{\omega_0}{\sqrt{1 + k_{12}}} \\ \omega_{high} &= \frac{\omega_0}{\sqrt{1 - k_{12}}} \end{aligned} \tag{4.14}$$

When the TX and RX are far apart, the coupling becomes weak and the two frequencies converge to the center resonant frequency ω_0.

4.2.2 Multiple-Input and Multiple-Output WPT System

In previous session, frequency splitting is investigated in the conventional SISO system and frequency modes are obtained from eigenvalue analysis. In this session, similar approach is used to examine the frequency characteristics of a MIMO system. Figure 4-5 [75] shows the equivalent circuit of a prototype MIMO system architecture that will be examined in experiments. In this system, two TXs and two RXs are coupled indirectly through the repeater. The repeater acts as a power hub to harvest power from two TXs and redistribute power to two RXs to achieve a high transfer efficiency, compared to the case of same transfer distance without a repeater [56]. The MIMO system can be modeled by using the impedance matrix equation:

$$\begin{bmatrix} Z_{11} & Z_{12} & Z_{13} & Z_{14} & Z_{15} \\ Z_{21} & Z_{22} & Z_{23} & Z_{24} & Z_{25} \\ Z_{31} & Z_{32} & Z_{33} & Z_{34} & Z_{35} \\ Z_{41} & Z_{41} & Z_{41} & Z_{41} & Z_{41} \\ Z_{51} & Z_{52} & Z_{53} & Z_{54} & Z_{55} \end{bmatrix} \begin{bmatrix} I_1 \\ I_2 \\ I_3 \\ I_4 \\ I_5 \end{bmatrix} = \begin{bmatrix} |V_1| \angle \theta_1 \\ |V_2| \angle \theta_2 \\ 0 \\ 0 \\ 0 \end{bmatrix} \tag{4.15}$$

Or

$$\underline{I} = \underline{Z}^{-1} \underline{V} \tag{4.16}$$

where $\underline{Z}$, $\underline{V}$, $\underline{I}$ are the impedance matrix, voltage and current vectors, respectively; θ_i is the phase of the source voltage at TX_i. In this research, voltage sources are chosen to be in phase with equal amplitudes. After obtaining current vectors from Eq. 4-16, input power, output power, normalized transfer power and transfer efficiency can be expressed, respectively, as:

$$\begin{aligned} P_{in} &= \frac{1}{2}\mathrm{Re}\left(V_1 I_1^*\right) + \frac{1}{2}\mathrm{Re}\left(V_2 I_2^*\right) \\ P_{out} &= |I_4|^2 R_{load\,4} + |I_5|^2 R_{load\,5} \\ P_{norm} &= \frac{P_{out}}{P_{in\_\max}}; \eta = \frac{P_{out}}{P_{in}} \end{aligned} \tag{4.17}$$

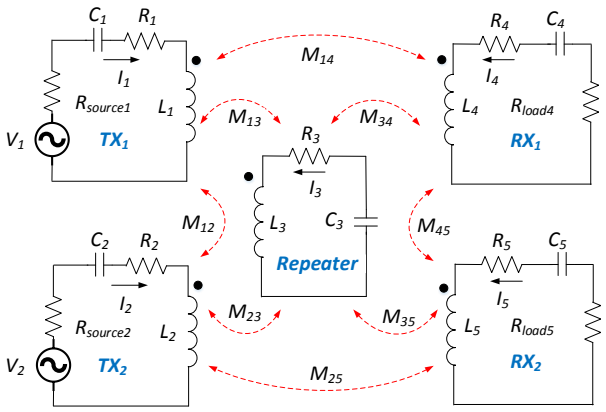

Figure 4-5 Equivalent circuit of the prototype MIMO WPT system

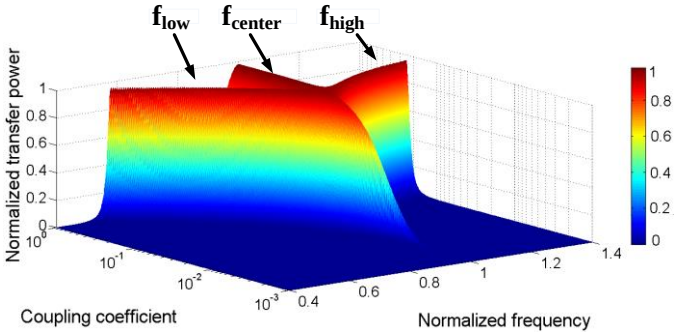

Figure 4-6 Normalized transfer power as a function of coupling coefficient and normalized frequency in the prototype MIMO system

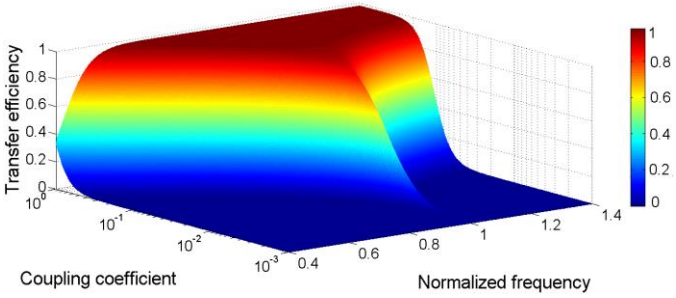

Figure 4-7 Transfer efficiency as a function of coupling coefficient and normalized frequency in the prototype MIMO system

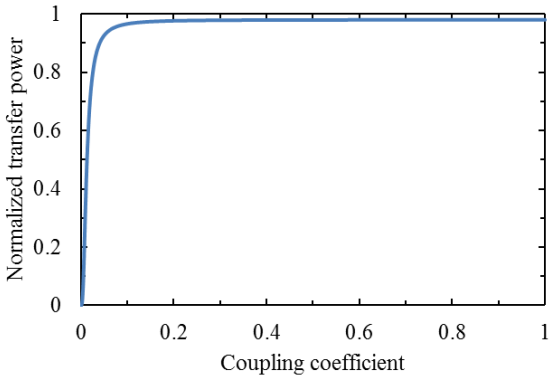

Figure 4-8 Normalized transfer power at the center frequency in the prototype MIMO system

Table 4-2 MIMO System Parameters

Parameter	Value
$R_{source1}$,$R_{source2}$	50 Ω
R_{load4},R_{load5}	50 Ω
Z_0	50 Ω
L_1,L_2,L_4,L_5	7 μH
L_3	11 μH
C_1,C_2,C_4,C_5	78.7 pF
C_3	50.1 pF
R_1,R_2,R_4,R_5 (DC)	0.5 Ω
R_3 (DC)	0.8 Ω
R_1,R_2,R_4,R_5 (AC)	3.8 Ω
R_3 (AC)	4.2 Ω

For simplicity, the direct coupling between a pair of TX and RX is sufficiently weak to be negligible while the coupling effects between the repeater and all other antennas are similar due to the symmetry of the antenna arrangement. Thus M_{14} are M_{25} are set as zero while $M_{13}=M_{23}=M_{34}=M_{35}$. The cross coupling between RXs and between TXs are also negligible with sufficient spacing [56]. Thus $M_{12}=M_{45}=0$. The system parameters are given in Table 4-2. Normalized transfer power and transfer efficiency are shown in Figs. 4-6 and 4-7 [75], respectively. Similar to the SISO system, transfer efficiency is always maximized at the center frequency which is the desired operating frequency with all elements tuned to it. However, the transfer power can be maximized at three different frequency modes. This can be explained as the rank of $\underline{A}$ in the MIMO system is greater than two. Therefore, $\underline{A}$ has more than two eigenvalues, or the system has more than two frequency modes. These modes will be discussed in details in the next section.

Figure 4-8 [75] shows the variation of transfer power as a function of the coupling coefficient at the center frequency. The transfer power is always maximized at the center frequency even in the over-coupled region. The presence of the center mode in addition to low- and high- frequency modes in this MIMO system creates a difference in frequency splitting from the conventional SISO system.

4.3 Experiments

Experiment setup with two TXs, two RXs and a repeater is built and measured to verify the analytical model. Antenna design is shown in Fig. 4-9 [75]. Antennas are fabricated on top of the FR4 substrates using photolithography and etching. The dielectric constant of FR4 is 4.8. The thickness of copper is 35 μm while the thickness of the substrate is 1.6 mm. TX and RX antennas are identical while the repeater antenna is larger in order to spatially cover all TX and RX. Antennas are spiral in rectangular shapes and

have 5 turns. Antenna dimensions are given in Table 4-3. Figure 4-10 [75] shows the antenna arrangement in the top view with detail spacings between antennas. Each pair of TX_1-RX_1 and TX_2-RX_2 is perfectly aligned center to center. The repeater is placed symmetrically between TX and RX so that the mutual coupling between the repeater and all other antennas are the same. That mutual coupling is measured at k=0.2 using the short- and open-circuit method [73]. Lump capacitors are used to tune each individual antenna at 6.78 MHz. Lump parameters are given in Table 2. Antenna resistance is measured in both DC and AC. AC load voltages are captured from the oscilloscope to calculate the output powers.

Table 4-3 Antenna Design

Parameter	Value
$s_{TX,RX}$	5 mm
$w_{TX,RX}$	5 mm
$h_{TX,RX}$	140 mm
$d_{TX,RX}$	140 mm
$s_{repeater}$	5 mm
$w_{repeater}$	5 mm
$h_{repeater}$	140 mm
$d_{repeater}$	380 mm

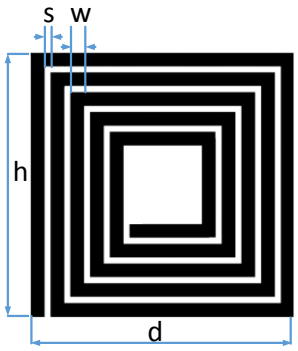

Figure 4-9 Antenna design for the MIMO system

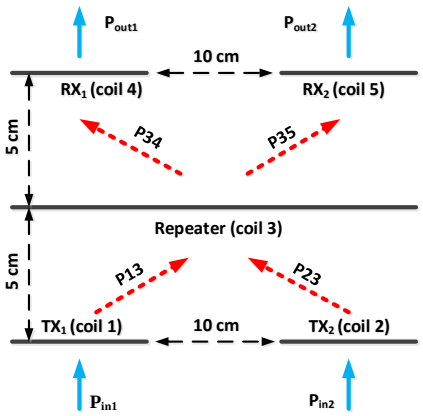

Figure 4-10 Antenna arrangement in top view and power flow diagram

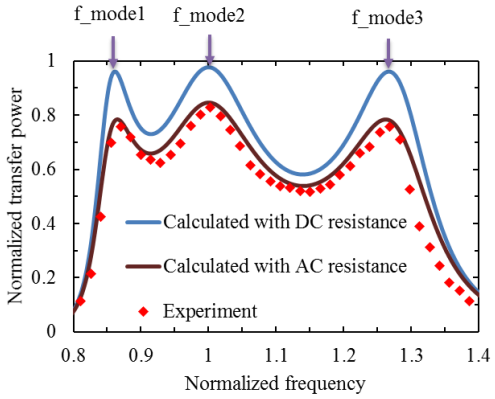

Figure 4-11 Calculated and measured normalized transfer power at k=0.2 in the MIMO system

Figure 4-11 [75] shows the frequency response for the transfer power at k=0.2. Measured output power is normalized to the maximum input power in order to compare with the analytical results. Different from the SISO system, the frequencies are split into three different modes.

Eigenvalue analysis is performed to obtain solutions for these frequency modes. The matrix A for the MIMO system is determined from Eq. 4.15 as:

$$\underline{A} = \begin{bmatrix} 1 & 0 & k_{13}\sqrt{L_3/L_1} & 0 & 0 \\ 0 & 1 & k_{23}\sqrt{L_3/L_2} & 0 & 0 \\ k_{13}\sqrt{L_1/L_3} & k_{23}\sqrt{L_2/L_3} & 1 & k_{34}\sqrt{L_4/L_3} & k_{35}\sqrt{L_5/L_3} \\ 0 & 0 & k_{43}\sqrt{L_3/L_4} & 1 & 0 \\ 0 & 0 & k_{35}\sqrt{L_3/L_5} & 0 & 1 \end{bmatrix}$$

Solving Eq. 4.12 at k=0.2, the eigenvalues of A are obtained as λ_1=0.64, λ_2=1 and λ_3=1.34. The center eigenvalue λ_2=1 is a triple-solution. This is due to TXs and RXs being identical. The corresponding frequency modes are f_{mode1}=0.86, f_{mode2}=1, f_{mode3}=1.25 and the actual frequency values are f_1=5.83 MHz, f_2=6.78 MHz and f_3=8.48 MHz, respectively. In terms of the frequency modes, the measured results match well with the theoretical ones. Additional losses from AC resistances, measured with the impedance analyzer at 6.78 MHz, are observed due to the skin and proximity effect of the multi-turn conductor at high frequencies [74]. The calculated curve with the measured AC resistances matches the measured data.

Similar to the SISO system, the above results are obtained with the assumption that the imaginary term *1/iQi* in the diagonal elements of A can be neglected, therefore, A is a matrix with only real coefficients. In practical conditions, the antenna might have low quality factors due to high RF resistance. In such cases, the imaginary term *1/iQi* might be significant and A will have complex coefficients, which results in complex eigenvalues as well as complex frequency modes. In order to examine this effect, practical values of the antenna resistance are taken into account and the corresponding complex frequency modes are given in Table 4-4. In “no loss” condition, frequency modes contain only real values. When the resistance increases, the imaginary parts start to show up and increase proportionally with the resistance. The imaginary part of the frequency modes can be considered as a damping factor representing insertion loss in the system.

Figure 4-12 Demonstration of the prototype MIMO system. The system is able to deliver 5 W to each light bulb connected to RXs with an overall transfer efficiency of 80% at 5.83 MHz, 6.78 MHz and 8.48 MHz

Table 4-4 Complex Frequency Modes in the MIMO System

$R_{TX,RX}$	$R_{repeater}$	f_{mode1}	f_{mode2}	f_{mode3}
0 Ω	0 Ω	0.86	1	1.25
0.5 Ω	0.8 Ω	0.86+0.027i	0.99+0.083i	1.23+0.081i
5 Ω	8 Ω	0.86+0.032i	0.99+0.090i	1.23+ .096i
10 Ω	16 Ω	0.86+0.037i	0.98+0.098i	1.23+0.111i
20 Ω	32 Ω	0.86+0.048i	0.98+0.113i	1.22+0.141i
30 Ω	48 Ω	0.85+0.058i	0.97+0.128i	1.21+0.169i
40 Ω	64 Ω	0.85+0.067i	0.97+0.143i	1.20+0.196i

The real part, on the other hands, seems to be invariant to the loss and represent the actual frequency peaks of the system, which shift slightly from the ones without loss.

Experimental demonstration for the MIMO system is shown in Fig. 4-12 [75]. In this setup, the distance between the repeater and TXs as well as RXs is 5 cm. The coupling coefficient between the repeater and all other antennas is measured at k=0.2. Load resistors are replaced by two 5-W LED light bulbs. Two light bulbs are turned on particularly at 5.83 MHz, 6.78 MHz and 8.48 MHz. The transfer efficiency is measured at 80%. This confirms the ability of the system to deliver maximum transfer powers at three different frequency modes in the over-coupled region.

4.4 Conclusions

In this work, the frequency splitting of both the SISO and MIMO wireless power transfer systems is examined. An experimental setup consisting of two TXs, two RXs and a repeater antennas is built to validate the theory model. Both analytical and experimental results confirm the multiple frequency modes in the MIMO system. These modes can be obtained directly using eigenvalue analysis. Regarding this approach, it is clear that the number of modes depend on the rank of the impedance matrix, or the number of antennas in the system. In our prototype MIMO system, there are three different modes including the center frequency mode. Therefore, the system can deliver maximum output power at the center frequency even in the over-coupled region.

References

[1] T. Ativanichayaphong, S. J. Tang, J. Wang, W. D. Huang, H. F. Tibbals, S. J. Spechler and J.-C. Chiao, “An Implantable, Wireless and Batteryless Impedance Sensor Capsule for Detecting Acidic and Non-Acidic Reflux,” *Gastroenterology*, Vol. 134, A-63, 2008.

[2] H. Cao, S. Rao, S. J. Tang, H. F. Tibbals, S. J. Spechler and J.-C. Chiao, “A Batteryless, Implantable, Dual-sensor Capsule for Gastroesophageal Reflux Monitoring,” *Gastrointestinal Endoscopy*, EPub, Jan. 2 2013.

[3] T. Ativanichayaphong, S. J. Tang, L. C. Hsu, W. D. Huang, Y. Seo, H.F. Tibbals, S. J. Spechler and J.-C. Chiao, “An Implantable Batteryless Wireless Impedance Sensor for Gastroesophageal Reflux Diagnosis," *IEEE International Microwave Symposium*, Anaheim, May 23-28, 2010.

[4] S. Deb, S. J. Tang, T. L. Abell, S. Rao, W. D. Huang, S. D. To, C. Lahr and J.-C. Chiao, “An Endoscopic Wireless Gastrostimulator (with video),” *Gastrointestinal Endoscopy*, Vol. 75, No. 2, pp. 411- 415, 2012.

[5] H. Cao, S. K. Thakar, T. Fu, M. Sheth, M. L. Oseng, V. Landge, Y. Seo, and J.-C. Chiao, “A Wireless Strain Sensor System for Bladder Volume Monitoring,” *IEEE International Microwave Symposium*, pp. 1-4, Baltimore, Jun. 5-10, 2011.

[6] K. M. Silay, C. Dehollain and M. A. Declercq, “Closed-Loop Remote Powering Link for Wireless Cortical Implants,” *IEEE Sensors Journal,* Vol. 13, Issue 9, pp. 3226-3235, 2013.

[7] S. Kim, J. S. Ho, L. Y. Chen and A. S. Poon, “Wireless Power Transfer to a Cardiac Implant,” *Applied Physics Letters*, Vol. 101, Issue. 7, pp. 073701 - 073701-04, Aug. 2012.

[8] M. Q. Nguyen, P. Woods, Y. Seo, S. Rao and J.-C. Chiao, “Position and Angular Misalignment Analysis for a Wirelessly Powered Stimulator,” *Proceedings of the IEEE International Microwave Symposium*, Seattle, Jun. 2-7, 2013.

[9] W. Wu and Q. Fang, “Design and Simulation of Printed Spiral Coil used in Wireless Power Transmission Systems for Implant Medical Devices,” *IEEE International Conference of Engineering in Medicine and Biology*, pp. 4018-4021, Aug. 30-Sep. 3, 2011.

[10] M. Lee, B. A. Kramer, C. C. Chen and J. L.Volakis, “Distributed Lumped Loads and Lossy Transmission Line Model for Wideband Spiral Antenna Miniaturization and Characterization,” *IEEE Transactions on Antennas and Propagation*, Vol. 55, Issue. 10, pp. 2671-2678, 2007.

[11] W. Smythe, “Static and Dynamic Electricity,” 2nd Edition, Mc-Graw Hill, pp. 270-271.

[12] M. Zolog, D. Pitica and O. Pop, “Characterization of Spiral Planar Inductors Built on Printed Circuit Boards,” *IEEE International Spring Seminar on Electronics Technology*, pp. 308-313, May. 2007.

[13] S. Babic, “The Mutual Inductance of Two Thin Coaxial Disk Coils in Air,” *IEEE Trans. Magn*, Vol. 40, No. 2, pp. 822–825, 2004.

[14] K. Schuylenbergh, “Inductive Powering Basic Theory and Application to Biomedical Systems,” Springer, 2009.

[15] X. L. Huang, H. Qiang, and L. L. Tan, “The Coil Misalignment Model of Inductively Coupled Wireless Power Transfer System: Mutual Inductance Analysis and Transfer Efficiency Optimization,” *Progress In Electromagnetics Research Symposium Proceedings*, Russia, pp. 679-683, Aug. 19-23, 2012.

[16] K. Fotopoulou and B.W. Flynn, “Wireless Power Transfer in Loosely Coupled Links: Coil Misalignment Model,” *IEEE Trans. Magn*, Vol. 47, No. 2, pp. 416-430, Feb. 2011.

[17] R. Selvakumaran, W. Liu, B. H. Soong, L. Ming and S. Y. Loon, “Design of Inductive Coil for Wireless Power Transfer,” *IEEE/ASME International Conference on Advanced Intelligent Mechatronics*, pp. 584-589, Singapore, Jul. 14-17, 2009.

[18] K. Jung, Y. H. Kim, E. J. Choi, H. Kim and Y. J. Kim, “Wireless Power Transmission for Implantable Devices Using Inductive Component of Closed-Magnetic Circuit Structure,” *International Conference on Multisensor Fusion and Integration for Intelligent System*, Seoul, Korea, pp. 272-277, Aug. 20 - 22, 2008.

[19] F. W. Grover, “Inductance Calculations, Working Formulas and Tables,” 2nd ed. New York: Van Nostrand, 1946.

[20] S. Kong, M. Kim, K. Koo, S. Ahn, B. Bae and J. Kim, “Analytical Expressions for Maximum Transferred Power in Wireless Power Transfer Systems,” *IEEE International Symposium on Electromagnetic Compatibility*, pp. 379-383, Aug. 2011.

[21] A. RamRakhyani, S. Mirabbasi and M. Chiao. “Design and Optimization of Resonance-Based Efficient Wireless Power Delivery Systems for Biomedical Implants,” *IEEE Trans. Biomed. Circuits Syst.*, Vol. 5, No. 1, pp. 48-63, Feb. 2011.

[22] R. R. Harrison. “Designing Efficient Inductive Power Links for Implantable Devices,” *International Symposium on Circuits and Systems*, pp. 2080-2083, 2007.

[23] X. Liu, F. Zhang, S. A. Hackworth, R. J. Sclabassi and M. Sun, “Wireless Power Transfer System Design for Implanted and Worn Devices,” *IEEE Annual Northeast Conference on Bioengineering*, pp. 1-2, Boston, Apr. 3-5. 2009.

[24] M. Soma, D. C. Galbraith and R. L. White, “Radio-Frequency Coils in Implantable Devices: Misalignment Analysis and Design Procedure,” *IEEE Trans. Biomed. Eng.*, Vol. 34 , Issue 4, pp. 276-282, 1987.

[25] U. M. Jow and M. Ghovanloo, “Design and Optimization of Printed Spiral Coils for Efficient Transcutaneous Inductive Power Transmission,” *IEEE Trans. Biomed. Circuits Syst.*, Vol. 1, No. 3, pp. 193-202, Sep. 2007.

[26] W. H. Ko, S. P. Liang, and C. D. F. Fung, “Design of Radio-Frequency Powered Coils for Implant Instruments,” *Med. Biol. Eng. Comput*, Vol.15, Issue 4, pp. 634-640, Nov. 1977.

[27] *2005 IEEE Standard for Safety Levels With respect to Human Exposure to Radio Frequency Electromagnetic Fields,* 3kHz to 300GHz, IEEE Std C95.1, 2006.

[28] A. Abdolkhani, A. P. Hu, M. Moridnejad and A. Croft, “Wireless Charging Pad based on Travelling Magnetic Field for Portable Consumer Electronics*,” IEEE 39th Conf. of Ind. Electronics*, pp. 1416-1421, Nov. 10-13, 2013.

[29] C. G. Kim, D. H. Seo, J. S. You, J. H. Park, and B. H. Cho, “Design of a Contactless Battery Charger for Cellular Phone,” *IEEE Trans. Ind. Electron*., Vol. 48, No. 6, pp. 1238–1247, Dec. 2001.

[30] Y. T. Jang and M. M. Jovanovic, “A Contactless Electrical Energy Transmission System for Portable-Telephone Battery Chargers,” *IEEE Trans. Ind. Electron*., Vol. 50, No. 3, pp. 520–527, Jun. 2003.

[31] Y. S. Seo, Z. Hughes, M. Hoang, D. Isom, M. Nguyen, S. Rao, and J.-C. Chiao, “Investigation of Wireless Power Transfer in Through-wall Applications,” *Asia-Pacific Microwave Conf.,* pp. 403-405, Dec. 4-7, 2012.

[32] O. Jonah and S. V. Georgakopoulos, “Wireless Power Transfer in Concrete via Strongly Coupled Magnetic Resonance,” *IEEE Trans. Antenna and Propagation*, Vol. 61, No. 3, pp. 1378-1384, Mar. 2013.

[33] M. Q. Nguyen, Z. Hughes, P. Woods, Y. S. Seo, S. Rao and J.-C. Chiao, “Field Distribution Models of Spiral Coil for Misalignment Analysis in Wireless Power Transfer Systems,” *IEEE Trans. on Microwave Theory & Tech*., Vol. 62, No. 4, pp. 920-930, Jan. 2014.

[34] Y. S. Seo, Z. Hughes, D. Isom, M. Q. Nguyen, S. Deb, S. Rao and J.-C. Chiao, “Wireless Power Transfer for a Miniature Gastrostimulator,” *European Microwave Conf.*, pp. 229-232, Oct. 28-Nov. 2, 2012.

[35] H. Cao,V. Landge, U. Tata,Y. Seo, S. Rao,S. J. Tang, H. F. Tibbals, S. J. Spechler, and J.-C. Chiao, “An implantable, Batteryless, and Wireless Capsule with Integrated Impedance and pH Sensors for Gastroesophageal Reflux Monitoring,” *IEEE Trans. Biomed. Eng*., Vol. 59, No. 11, pp. 3131-3199, Nov. 2012.

[36] R. Wu, W. Li, H. Luo, J. K. O. Sin and C. C. Yue, “Design and Characterization of Wireless Power Links for Brain -Machine Interface Applications,” *IEEE Trans. Power Electron.,* Vol. 29, No. 10, pp. 5462-5471, Oct. 2014.

[37] A. RamRakhyani, S. Mirabbasi and M. Chiao, “Design and Optimization of Resonance-Based Efficient Wireless Power Delivery Systems for Biomedical Implants,” *IEEE Trans. Biomed. Circuits Syst*., Vol. 5, No. 1, pp. 48-63, Feb. 2011.

[38] S. Aldhaher,P. C. -K. Luk and J. F. Whidborne, “Electronic Tuning of Misaligned Coils in Wireless Power Transfer Systems,” *IEEE Trans. Power Electron.,* Vol. 29, No. 11, pp. 5975-5982, Nov. 2014.

[39] A. Kurs, A. Karalis, R. Moffatt, J. D. Joannopoulos, P. Fisher, and M. Soljacic, “Wireless Power Transfer via Strongly Coupled Magnetic Resonances,”*Sci. Express*, Vol. 317, No. 5834, pp. 83–86, Jul. 2007.

[40] S. Y. R. Hui, W. Zhong and C. K. Lee, “A Critical Review of Recent Progress in Mid-Range Wireless Power Transfer,” *IEEE Trans. Power Electron.,* Vol. 29, No. 9, pp. 4512-4520, Sep. 2014.

[41] Y. Zhang, Z. Zhao and K. Chen, “Frequency Decrease Analysis of Resonant Wireless Power Transfer,” *IEEE Trans. Power Electron.,* Vol. 29, No. 3, pp. 1058-1063, March 2014.

[42] Y. Lim, H. Tang, S. Lim and J. Park, “An Adaptive Impedance-Matching Network Based on a Novel Capacitor Matrix for Wireless Power Transfer,” *IEEE Trans. Power Electron.,* Vol. 29, No. 8, pp. 4403-4413, Aug. 2014.

[43] S. Kong, M. Kim, K. Koo, S. Ahn, B. Bae and J. Kim, “Analytical Expressions for Maximum Transferred Power in Wireless Power Transfer Systems,” *IEEE International Symposium on Electromagnetic Compatibility*, pp. 379-383, Aug. 2011.

[44] C. Park, S. Lee, G.-H. Cho and C. T. Rim, “Innovative 5-m-Off-Distance Inductive Power Transfer Systems With Optimally Shaped Dipole Coils,” *IEEE Trans. Power Electron*., Vol. 30, No. 2, pp. 817-827, Feb. 2015.

[45] I.-J. Yoon and H. Ling, “Investigation of Near-field Wireless Power Transfer under Multiple Transmitters,” *IEEE Antennas Wireless Propag. Lett*., Vol. 10, pp. 662-665, Jul. 2011.

[46] K. Lee and D. H. Cho, “Diversity Analysis of Multiple Transmitters in Wireless Power Transfer System,” *IEEE Trans. Magn*., Vol. 49, No. 6, pp. 2946-2952, Jun. 2013.

[47] A. Kurs, R. Moffatt, and M. Soljacic, “Simultaneous Mid-range Power Transfer to Multiple Devices,” *Appl. Phys. Lett.,* Vol. 96, No. 4, p. 044102, Jan. 2010.

[48] B. L. Cannon, J. F. Hoburg, D. D. Stancil, and S. C. Goldstein, “Magnetic Resonant Coupling as a Potential Means for Wireless Power Transfer to Multiple Small Receivers,” *IEEE Trans. Power Electron*., Vol. 24, No. 7, pp. 1819-1826, Jul. 2009.

[49] J. Kim, H.-C. Son, D.-H. Kim and Y.-J. Park, “Impedance matching considering cross coupling for wireless power transfer to multiple receivers,” *IEEE Wireless Power Transfer (WPT)*, pp. 226-229, Perugia, Italy, May 15-16, 2013.

[50] W. M. Ng, C. Zhang, D. Lin and S. Y. H. Rui. “Two- and Three-Dimensional Omnidirectional Wireless Power Transfer,” *IEEE Trans. Power Electron*., Vol. 29, No. 9, pp. 4475-4478, Sep. 2014.

[51] M. Q. Nguyen, D. Plesa, S. Rao and J.-C. Chiao, “A Multi-Input and Multi-Output Wireless Energy Transfer System,” *IEEE MTT-S Int. Microw. Symp. Dig*., Tampa, Florida, USA, Jun. 1-6, 2014.

[52] C. Lee, W. Zhong amd S. Hui, “Effects of Magnetic Coupling of Nonadjacent Resonators on Wireless Power Domino-Resonator Systems,” *IEEE Trans. Power Electron*., Vol. 27, No. 4, pp. 1905-1916, Apr. 2012.

[53] W. Zhong, C. Lee and S. Hui, “General Analysis on the Use of Tesla's Resonators in Domino Forms for Wireless Power Transfer,” *IEEE Trans. on Ind. Electronics*., Vol. 60, No. 1, pp. 261-270, 2013.

[54] S. I. Babic and C. Akye, “Calculating Mutual Inductance Between Circular Coils With Inclined Axes in Air,” *IEEE Trans. Magn.,* Vol. 44, No. 7, pp. 1743-1750, July 2008.

[55] S. Raju, R. Wu; M. Chan and C. P. Yue, “Modeling of Mutual Coupling Between Planar Inductors in Wireless Power Applications,” *IEEE Trans. Power Electron*., Vol. 29, No.1, pp. 481-490, Jan. 2014.

[56] M. Q. Nguyen, Y. Chou, D. Plesa, S. Rao and J.-C. Chiao, “Multiple Inputs and Multiple Outputs Wireless Power Combining and Delivering Systems,” *IEEE Transactions on Power Electronic*s, Vol. 30, No. 11, pp. 6254-6263, Jun. 2015.

[57] M. Q. Nguyen, D. Khoroshansky, S. Luce, O. Osasona, N. Joshi, S. Rao and J.-C. Chiao, “A Study of Coil Orientations to Enhance the Transfer Efficiency of a Multi-Repeater Wireless Power Transmission System,” *Asia-Pacific Microwave Conf.,* Nov. 4-7, 2014.

[58] M. Q. Nguyen, S. Dubey, S. Rao and J.-C. Chiao, “Wireless Power Transfer via Air and Building Materials Using Multiple Repeaters,” *Texas Symposium on Wireless & Microwave Circuits & Systems*, Waco, USA, Apr. 3-4, 2014.

[59] M. Q. Nguyen, P. Woods, Z. Hughes, Y. S. Seo, S. Rao and J.-C. Chiao “A Mutual Inductance Approach for Optimization of Wireless Energy Transmission,” *Texas Symposium on Wireless & Microwave Circuits & Systems*, Waco, USA, Apr. 3-4, 2014.

[60] C. M. Nguyen, P. Kota, M. Q. Nguyen, S. Dubey, S. Rao, J. Mays and J.-C. Chiao, “Wireless Power Transfer for Autonomous Wearable Neurotransmitter Sensors,” *Sensors*, Vol. 15, No. 9, pp. 24553-24572, Sep. 2015.

[61] S. Rao, S. Dubey, S. Deb, Z. Hughes, Y.-S. Seo, M. Q. Nguyen, S.-J. Tang, T. Abell, C. Lahr and J.-C. Chiao, “Wireless Gastric Stimulators,” *Texas Symposium on Wireless & Microwave Circuits & Systems*, Waco, TX, April 3-4 2014.

[62] C. M. Nguyen, J. Mays, D. Plesa, S. Rao, M. Q. Nguyen and J.-C. Chiao, “Wireless Sensor Nodes for Environmental Monitoring in Internet of Things,” *IEEE International Microwave Symposium*, Phoenix, USA, Jun. 1-6, 2015.

[63] Y. Seo, M. Q. Nguyen, Z. Hughes, S. Rao and J.-C. Chiao, “Wireless power transfer by inductive coupling for implantable batteryless stimulators,” *IEEE International Microwave Symposium,* Montreal Canada, Jun. 17-22, 2012.

[64] Z. Hughes, Y. Seo, P. Woods, M. Q. Nguyen, S. Rao, P. McCorkle, and J-C. Chiao “Mapping Wireless Power Transfer for Implantable Stimulator Applications,” *BMES Annual Meeting*, Seattle, USA, Sep. 25-28, 2013.

[65] A. P. Sample, D. A. Meyer and J. R. Smith, “Analysis, Experimental Results, and Range Adaptation of Magnetically Coupled Resonators for Wireless Power Transfer,” *IEEE Trans. Ind. Electron*., Vol. 58, No. 2, pp. 544–554, Feb. 2011.

[66] T. Imura and Y. Hori, “Maximizing air gap and efficiency of magnetic resonant coupling for wireless power transfer using equivalent circuit and Neumann formula,” *IEEE Trans. Ind. Electron*., Vol. 58, No. 10, pp. 4746–4752, Oct. 2011.

[67] Y. Zhang and Z. Zhao, “Frequency Splitting Analysis of Two-Coil Resonant Wireless Power Transfer,” *IEEE Antennas Wireless Propag. Lett*., Vol. 13, pp. 400-402, March. 2014.

[68] Y. Zhang and Z. Zhao, “Frequency-Splitting Analysis of Four-Coil Resonant Wireless Power Transfer,” *IEEE Trans. Ind. Appl*., Vol. 50, No. 4, pp. 2436-2445, Aug. 2014.

[69] R. Huang, B, Zhang, D. Qiu and Y. Zhang, “Frequency Splitting Phenomena of Magnetic Resonant Coupling Wireless Power Transfer,” *IEEE Trans. Magn*., Vol. 50, No. 11, Nov. 2014.

[70] D. Ahn and S. Hong, “Effect of Coupling Between Multiple Transmitters or Multiple Receivers on Wireless Power Transfer,” *IEEE Trans. Ind. Electron*., Vol. 60, No. 7, pp. 2602–2613, Jul. 2013.

[71] H. Nguyen and J. I. Agbinya, “Splitting Frequency Diversity in Wireless Power Transmission,” *IEEE Trans. Power Electron*., Vol. 30, No. 11, pp. 6088-6096, Nov. 2015.

[72] O. Karaca, F. Kappeler, D. Waldau, R. M. Kennel and J. Rackles, “Eigenmode Analysis of a Multiresonant Wireless Energy Transfer System,” *IEEE Trans. Ind. Electron*., Vol. 61, No. 8, pp. 4134–4141, Aug. 2014.

[73] S. Hackl, C. Lanschutzer, P. Raggam and W. L. Randeu, “A Novel Method for Determining the Mutual Inductance for 13.56 MHz RFID systems,” International Symposium Com. Sys., Net. and DSP., pp. 297-300, Jul. 2008.

[74] Y. Zhilichev, “Analysis of Eddy Currents in Rectangular Coils by Integral Equation Method in Sub-Domains,” *IEEE Trans. Magn*., Vol. 50, No. 12, Dec. 2014.

[75] M. Q. Nguyen, K. Ta, S. Dubey and J.-C. Chiao, “Frequency Modes in a MIMO Wireless Power Transfer System,” *IEEE Trans. Magn*., (submitted)

Biographical Information

Minh Nguyen received his Bachelor and Master degree in Electrical Engineering from Hanoi University of Science and Technology in 2007 and 2009, respectively. He earned his PhD degree in Electrical Engineering at the University of Texas at Arlington in 2016. His current research interests include microwave & RF design of wireless systems, electromagnetic wave propagation, power converter, implantable electronic devices, power system protection and the integration of renewable energy into power systems.